Interacting rhythms enhance sensitivity of target detection in a fronto-parietal computational model of visual attention

Amélie Aussel[1,2*], **Ian C. Fiebelkorn**[3,4], **Sabine Kastner**[4,5], **Nancy J. Kopell**[1,2†], **Benjamin R. Pittman-Polletta**[1,2†]

***For correspondence:** aaussel@bu.edu (AA)

†Supervising author

[1]Cognitive Rhythms Collaborative, Boston University; [2]Department of Mathematics and Statistics, Boston University; [3]Department of Neuroscience and Del Monte Institute for Neuroscience, University of Rochester Medical Center, University of Rochester; [4]Princeton Neuroscience Institute, Princeton University; [5]Department of Psychology, Princeton University

Abstract Even during sustained attention, enhanced processing of attended stimuli waxes and wanes rhythmically, with periods of enhanced and relatively diminished visual processing (and subsequent target detection) alternating at 4 or 8 Hz in a sustained visual attention task. These alternating attentional states occur alongside alternating dynamical states, in which lateral intraparietal cortex (LIP), the frontal eye field (FEF), and the mediodorsal pulvinar exhibit different activity and functional connectivity at α, β, and γ frequencies—rhythms associated with visual processing, working memory, and motor suppression. To assess whether and how these multiple interacting rhythms contribute to periodicity in attention, we propose a detailed computational model of FEF and LIP, which reproduced the rhythmic dynamics and behavioral consequences of observed attentional states when driven by θ-rhythmic inputs simulating experimentally-observed pulvinar activity. This model reveals that the frequencies and mechanisms of the observed rhythms allow for peak sensitivity in visual target detection while maintaining functional flexibility.

Introduction

The term 'selective attention' refers broadly to a set of neural mechanisms that are tailored to boost the processing of behaviorally relevant stimuli, allocating the brain's limited processing capacity in an efficient way. Classically, it has been assumed that attention-related modulation of sensory processing is continuous over time during attentional deployment. However, there is now mounting evidence that, even during sustained attention, the attentional enhancement of visual processing waxes and wanes over time (***Benedetto et al., 2020***; ***Fiebelkorn and Kastner, 2019b***). In a sustained visual attention task, periods of enhanced sensory processing at an attended location alternate with periods of relatively diminished sensory processing, at a rate of 4–8 cycles per second (i.e., in the θ frequency range, ***Fiebelkorn and Kastner*** (***2019b***)).

This rhythmic sampling of the visual environment is apparent at the behavioral level: measuring the success of target detection as a function of the interval between presentation of a spatially predictive cue and a target reveals an oscillation in hit rates with 8 Hz periodicity at the cued location and 4 Hz periodicity at the uncued location (***Fiebelkorn et al., 2018***, ***2013***; ***Landau and Fries,***

2012; *Song et al., 2014*; *VanRullen et al., 2007*). Monkey and human electrophysiology has linked this rhythmicity in spatial attention to neural activity in various nodes of the attention network (*Fiebelkorn et al., 2018*, *2019*; *Gaillard et al., 2020*; *Helfrich et al., 2018*). Recordings from the frontal eye field (FEF) and lateral intraparietal area (LIP) in monkeys have revealed that θ-rhythmic changes in behavioral performance are associated with θ phase-dependent attentional states, which alternate at 4 Hz and are characterized by distinct neural dynamics and distinct patterns of functional connectivity between these areas (*Fiebelkorn et al., 2018*, *2019*). These alternating states are also characterized by differences in thalamo-cortical interactions, with the pulvinar—a higher order thalamic nucleus associated with cognitive functions including attention (*Halassa and Kastner, 2017*; *Fiebelkorn and Kastner, 2019a*; *Kastner et al., 2020*; *Saalmann and Kastner, 2011*) and interconnected with the cortical nodes of the attention network (including LIP and FEF) in monkeys (*Gutierrez et al., 2000*; *Romanski et al., 1997*; *Selemon and Goldman-Rakic, 1988*)—specifically coordinating cortical activity during the θ phase associated with enhanced perceptual sensitivity (the "good θ phase"), but not during the θ phase associated with relatively diminished perceptual sensitivity (the "poor θ phase") (*Fiebelkorn et al., 2019*).

The differences in circuit dynamics and functional connectivity observed during the good and poor θ phases suggest that, even during sustained attentional deployment, the attention system alternates between two states subserving different functional roles. Besides directing attention-related boosts in sensory processing, the attention network also coordinates orienting movements of the body (e.g., head movements) and eyes (e.g., saccadic eye movements) (*Corbetta et al., 1998*; *Moore and Fallah, 2001*). *Fiebelkorn and Kastner* (*2019b*) have proposed that rhythmic sampling reflects the temporal coordination of these sensory and motor functions, helping to avoid potential functional conflicts. That is, periodic dips in perceptual sensitivity (i.e., during the poor θ phase) may be associated with windows of opportunity for the motor system, during which it is easier to shift attention from the presently attended location to another location. Rhythmic sampling may thus provide critical cognitive flexibility, preventing excessive attention to any single stimulus in the environment.

Despite the appeal of this hypothesis, the neuronal circuit mechanisms that underlie the alternating dynamical and attentional states observed during sustained attention remain unknown—as does whether and how their mechanisms contribute to the suppression and enhancement of sensory processing and motor execution. While the good θ phase is characterized by a parietal-driven increase in γ-band (~30–90 Hz) activity and a frontal-driven increase in β_2-band (~20–30 Hz) activity, the poor θ phase is characterized by increased parietal β_1-band (~12–20 Hz) activity (*Fiebelkorn et al., 2018*, *2019*). Notably, γ-band activity has often been associated with enhanced sensory processing (*Fries, 2009*), and β_2-band activity has often been associated with the suppression of motor processing (*Gregoriou et al., 2012*; *Pogosyan et al., 2009*; *Zhang et al., 2008*). Consistent with these functional interpretations, during rhythmic sampling, γ-band activity is linked to LIP visual neurons (i.e., neurons that respond to visual stimulation but demonstrate no saccade-related activity), while β_2-band activity is linked to FEF visual-movement neurons (i.e., neurons that both respond to visual stimulation and demonstrate saccade-related activity, *Fiebelkorn et al.* (*2018*)). Circuit mechanisms associated with these rhythms have been implicated in sensory processing, attention, and working memory (*Kramer et al., 2008*; *Gelastopoulos et al., 2019*; *Lee et al., 2013*), but whether these mechanisms play a role in the complex rhythmic dynamics of the visual attention network is not known. In this study, we sought to leverage detailed information about neural dynamics during rhythmic sampling as well as insights from previous computational models to address the following questions: What are the mechanisms that generate the γ, β_2, and β_1 oscillations observed in LIP and FEF, and how do these mechanisms and oscillations interact? How is this oscillatory activity flexibly controlled to vary with the θ rhythm, and how does it contribute to function? In particular, can FEF and LIP oscillations explain the variation in behavioral performance over the θ cycle? Finally, are the specific frequencies observed in FEF and LIP, and the θ-frequency timing of these alternating attentional states, functionally significant?

To address these questions, we built and tested a computational model of FEF and LIP, representing the temporal dynamics of visual processing at a single location (on a single object), following the presentation of an attention-priming spatial cue. We leave the allocation of attention among multiple objects for future work. In our model, FEF and LIP were both driven θ-rhythmically by simulated mdPul input at α frequency. This is consistent with the experimental observation that mdPul exerts a Granger causal influence over FEF and LIP at an α frequency during a part of each θ cycle (i.e., at a particular phase of the θ rhythm; ***Fiebelkorn et al.*** (***2019***)). The model was constructed from biologically detailed neurons and is consistent with the known anatomy, physiology, and function of frontal and parietal circuits. It highlights the cell types and connections necessary to produce the dynamics of interest, to allow realistic insights into the mechanisms underlying these dynamics and their functional consequences, while also avoiding excessive complexity. That is, while other cell types and connections, besides those modeled, are present in the brain and may play important roles in other tasks and other aspects of this task, the present model suggests that the activity of these cell types plays a minimal role in the phenomena of interest (see Discussion, Modeling Choices & Limitations). Since small models with single-compartment neurons can be difficult to parameterize using electrophysiological measurements, we built on previous cortical models that reproduced experimentally observed network dynamics in other cognitive and physiological contexts—specifically, in the context of working memory and cholinergic neuromodulation (***Kramer et al., 2008***; ***Lee et al., 2013***; ***Gelastopoulos et al., 2019***). Incorporating these models as modules in our network increases the realism and explanatory power of our model, by further constraining its dynamics and function to match experimental observations.

Our model shows how θ-rhythmic input from the mediodorsal pulvinar (mdPul) to cortex, subsequent to a spatially informative cue, can produce alternating dynamical regimes that, in turn, explain periodicity in behavioral outcomes (i.e., hit rates). In a simulated sustained attention task, the model replicated the γ, β_2, and β_1 dynamics observed experimentally. It offered an explanation for the frequency-specific causal interactions between LIP and FEF, suggesting a progression during enhanced stimulus processing in which pulvinar input activates FEF and prepares LIP to respond, but top-down β_2 input from FEF is necessary to elicit a γ-rhythmic response from LIP. The model also replicated behavioral results, unexpectedly revealing how an 8 Hz behavioral oscillation (at the cued location) can arise from a 4 Hz alternation of attentional states, in dependence on the strength of functional connectivity from LIP to FEF. We found that altering the frequency of the underlying θ rhythm, or of the higher-frequency FEF or LIP oscillations, resulted in decreased task performance, providing evidence for the functional significance of these rhythmic dynamics. Finally, we found that model behavior was robust to some changes in model parameters, yet produced qualitatively distinct dynamics—characterized by different rhythms—in response to other parameter changes, which we hypothesize may represent other functional states of FEF and LIP. Thus, our results demonstrate the computational advantages of biologically realistic rhythmic network dynamics, suggesting that they enable visual attention networks to participate in attentional, motor, and cognitive tasks with sensitivity, flexibility, and versatility.

Results

We modeled LIP and FEF activity during a sustained attention task based on the Egly-Driver task (***Fiebelkorn et al.*** (***2019***), see Figure 1A). In this task, the participant (e.g., monkey) must release a lever when they detect a near-threshold contrast change in a visual scene. A trial begins when the participant fixates on the center of a screen and holds down a lever, and is presented with two horizontal bars. After a short delay, a visual cue appears at the end of one of the bars. The target has a 78% chance of appearing at the same location as the cue, and an 11% chance of appearing at one of the two bar ends adjacent to the cued location (locations A and C in Figure 1A). After another delay of random duration lasting between 0.3s and 1.6s, the target appears in the form of a near-threshold change in contrast at the end of one of the bars, lasting 0.1s. If the participant successfully detects the target, it then releases the lever to receive a reward. Hit rates for this task

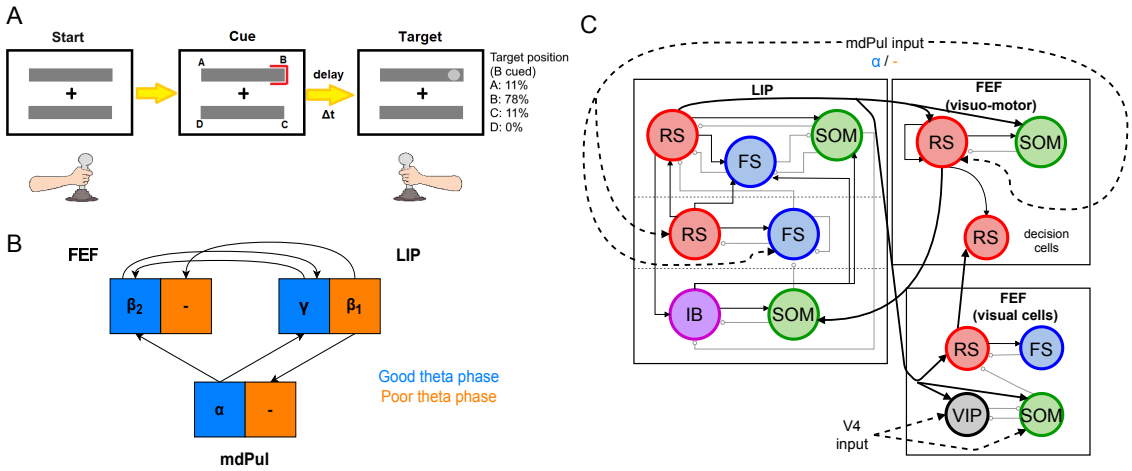

Figure 1. A. Schematic of the Egly-driver task modeled. B. Neuronal rhythms experimentally measured in FEF, LIP and mdPul during the task. C. Diagram of the full LIP and FEF model. Black lines ending in arrows and gray lines ending in circles indicate excitatory and inhibitory (chemical) synapses, respectively. Thick lines indicate synapses between modules. Dashed lines indicate synthetic inputs from regions that are not modeled. The mdPul input is at an alpha frequency during the good θ phase and is absent in the poor θ phase. RS: regular spiking pyramidal neurons. IB: intrinsic bursting pyramidal neurons. FS: fast-spiking (e.g., parvalbumin-positive) inhibitory interneurons. SOM: somatostatin-positive interneurons. VIP: vasoactive intestinal peptide-positive interneurons.

can be analyzed as a function of the time of target presentation (relative to cue presentation), and were found to exhibit θ-band periodicity, with alternating "good" and "poor" θ phases associated with increased and decreased hit rates, respectively, appearing at 4 Hz for the uncued object and 8 Hz for the cued object (***Fiebelkorn et al., 2013***, ***2019***).

Three of the different brain regions involved in the task, the Frontal Eye Field (FEF), the Lateral Intraparietal area (LIP) and the medio-dorsal pulvinar (mdPul), showed distinct patterns of activity between the good and poor θ phases (Figure 1B). During the good θ phase (coded in blue in Figure 1B and throughout), power spectra, Granger causality, spike-field coherence, and cross-frequency coupling indicated that: mdPul provided α-rhythmic (10-15 Hz) drive to FEF and LIP; FEF generated β_2 oscillations (20-30 Hz) that drove LIP; and LIP generated γ oscillations (>30Hz) that drove FEF. During the poor θ phase (coded in orange in Figure 1B and throughout), LIP produced dynamics at β_1 frequencies ($\sim$ 12 Hz). LIP β_1 activity was Granger causal to activity in mdPul and FEF, even though these regions did not exhibit robust activity at any specific frequency during the poor θ phase (***Fiebelkorn et al., 2019***).

Figure 1C shows the basic anatomy of the model. For LIP, we used a laminar model motivated by previous work on attention and memory (***Kramer et al., 2008***; ***Lee et al., 2013***; ***Gelastopoulos et al., 2019***). The model's dynamic repertoire of β_1, β_2, and γ rhythms depends on lamina-specific physiological properties and their interaction or isolation: superficial and deep layers can coordinate to produce a β_1 rhythm, while an input layer generates a γ rhythm and propagates it to the superficial layers. There are (at least) three different functional classes of pyramidal cells in FEF, typically classified based on their sensory- and saccade-related response profiles. Visual neurons exhibit sensory-related responses, movement neurons exhibit saccade-related responses, and visual-movement neurons exhibit both sensory and saccade-related responses (***Fiebelkorn et al., 2019***). In the experimental data we model here, too few FEF motor neurons were identified to draw reliable conclusions about their dynamics during the task (***Fiebelkorn et al., 2018***, ***2019***). Thus, we modeled FEF with two different functional modules: a visual module and a visuo-motor module. We remain agnostic about the relationships of these functional modules to the laminar structure of FEF, since the geometry of FEF complicates laminar recording and, thus, the laminar properties of FEF rhythms are not clear.

All cell types were modeled as Hodgkin-Huxley point neurons, with spiking (i.e. leak, sodium, and potassium) currents tailored with cell type-specific parameters (see Tables 1, 2, 3, 4, and 5

in Methods). In addition to two types of pyramidal cells (regular-spiking (RS) and deep intrinsic bursting (IB)), we modeled three types of interneurons. Parvalbumin positive interneurons were modeled as fast spiking (FS), and produced fast decaying inhibition (with a timescale of $5ms$), capable of pacing γ oscillations in networks consisting of interacting FS and RS cells. Somatostatin positive (SOM) interneurons contained an h-current in addition to the spiking current, and produced slower decaying inhibition (with a timescale of $20ms$, ***Silberberg and Markram*** (***2007***)), leading to β_2 oscillations when interacting with RS cells. Finally, vasoactive intestinal peptide (VIP) interneurons were modeled with a potassium D-current, and produced inhibition with a similar decay time to SOM cells, but spiked in response to much lower levels of excitation (Figure S1), in accordance with experimental data (***Tremblay et al., 2016***). VIP inhibition exclusively targets SOM interneurons in our model (see Methods).

All neurons in the model received tonic excitation at cell type-specific levels, encapsulating the effects of cell type-specific resting membrane potentials and/or background inputs (that do not vary with θ phase) from other brain regions. Each cell also received some random, gaussian-like excitation, and was initiated with a random membrane potential close to its resting potential (see Table 6). Certain cell types also received simulated input, designed to match mdPul drive during the cue-target interval. When isolated modules were analyzed, we substituted simulated inputs for the inputs that would arise from connected modules, based on the dynamics of those modules.

The rest of the Results section is organized as follows. In Mechanisms of FEF and LIP Oscillations During the Cue-Target Interval, we discuss model behavior during the cue-target interval and show that, when driven by θ-rhythmic inputs from mdPul and V4, the model reproduces the rhythms experimentally observed in LIP and FEF during both good and poor θ phases. In Mechanisms of Target Detection, we discuss model behavior on target presentation and show how the FEF model enables enhanced sensitivity and discrimination in target detection. In Task Performance, we share results on the functional implications of the model, and show the importance of the rhythms it generates. Finally, in Model Robustness and Flexibility, we discuss how parameters affect the model behavior, allowing it to exhibit different rhythms and possibly different functional states.

Mechanisms of FEF and LIP Oscillations During the Cue-Target Interval

To model the period between cue and target presentation in the Egly-Driver task (***Fiebelkorn et al., 2013***), we introduced simulated mdPul input—consisting of bursts of α frequency (12 Hz) excitation arriving during half of each period of a (4 Hz) θ rhythm—targeting LIP granular layer RS and FS cells, and FEF visuo-motor VIP cells. Under these conditions, the model reproduced the nested rhythmic dynamics observed experimentally (Figure 2B): during mdPul excitation (the putative good θ phase), FEF visuo-motor cells produced a β_2 rhythm, and LIP produced a γ rhythm; during mdPul quiescence (the putative poor θ phase), LIP produced β_1-frequency rhythmicity. Note that in the absence of additional visual input to FEF visual cells (i.e., when no target was present on screen), these cells and FEF decision cells (not shown in Figure 2) were relatively quiet. Below, we explain the circuit mechanisms of these rhythms and their interactions in detail for each module.

LIP Produces β_1 Oscillations Through Period Concatenation, and γ Oscillations When Stimulated by FEF and mdPul

The LIP module (Figure 3A) combined two previous laminar models of working memory and attention (***Kramer et al., 2008***; ***Lee et al., 2013***). The first of these was a model of a β_1 rhythm observed in rodent parietal slices (***Kramer et al., 2008***), shown to be useful for retention and manipulation of cell assemblies after the fading of a sensory input (***Gelastopoulos et al., 2019***). The model mimics experimental data (***Roopun et al., 2008***) in which adequate stimulation (sensory *in vivo*, excitatory agonist kainate *in vitro*) produced a γ rhythm in the superficial layers and an independent β_2 ($\sim$ 25Hz) rhythm in the deep layers. Following a sufficient period of kainate application *in vitro*, the removal of kainate (modeling the disappearance of the sensory signal) caused both deep and superficial layers to switch to a β_1 ($\sim$ 15 Hz) rhythm (***Roopun et al., 2008***). A

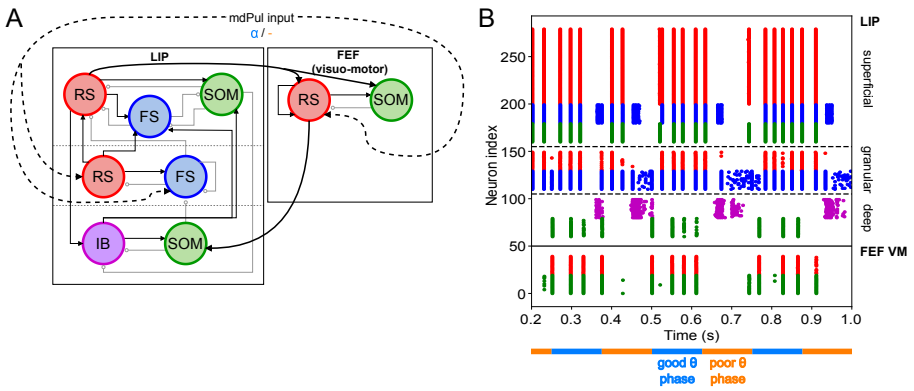

Figure 2. Model activity during the cue-target interval. Only the relevant modules and cell types are shown. **A. Diagram of the LIP and FEF visuo-motor module model (without decision cells).** Symbols are as in Figure 1C. **B. The LIP and FEF visuo-motor modules reproduce experimentally observed rhythms when driven by mdPul.** Raster plot from a 1-second long simulation with an alternation of good and poor θ phase pulvinar inputs. The activity of LIP is shown on top, and that of the FEF visuo-motor module at the bottom. No target was presented. LIP produces an alternation of γ and β_1 rhythms. FEF visuo-motor cells produce β_2 oscillations only during the good θ phase.

single period of this β_1 rhythm concatenated a single γ period and a single β_2 period (***Roopun et al., 2008***; ***Kramer et al., 2008***), so that the duration of the β_1 period was the sum of the γ and β_2 periods.

Both the γ period and the β_2 period comprising the β_1 are initiated by rebound from inhibition; this allows the β_1 to remain active even at low levels of excitatory input (***Kramer et al., 2008***). As a consequence of the unusual physiology producing it, this rhythm exhibits unique functional properties: a superficial γ-rhythmic cell assembly excited by an initial stimulus maintains persistent activity as part of a β_1 rhythm after the cessation of the initial stimulus; and multiple cell assemblies can be added and subtracted from this “working memory buffer" without interference (***Gelastopoulos et al., 2019***). Thus, this model is especially relevant to our task, which involves maintaining the cue location in working memory for up to $1.6s$, until target appearance.

Of note, the prior excitation required to produce the β_1 rhythm experimentally did not change the β_2 or γ rhythms during the period of excitation, but was hypothesized to produce plasticity altering interlaminar interactions. Such plasticity would occur *in vivo* either more rapidly during stimulation or in response to repeated stimulation. In computational models (***Kramer et al., 2008***; ***Gelastopoulos et al., 2019***), the parameters were set as if this plasticity had already occurred; thus the shift from independent γ and β_2 rhythms to a β_1 rhythm required only a change in the inputs to the model.

The second inspiration for the LIP module was a model of the effects of (attentional) cholinergic modulation on the potentiation of γ power in the superficial layers of sensory cortex (***Lee et al., 2013***). In this model, the excitation-inhibition balance in the granular layers is such that FS cells dominate RS cells, largely damping RS cell responses to excitatory input. In the presence of cholinergic modulation, beta rhythms delivered to deep layers activate SOM interneurons, which in turn produce slowly decaying inhibition that suppresses granular layer FS cells. This results in disinhibition of granular layer RS cells, changing the excitation-inhibition balance sufficiently that RS cells drive FS cells to produce a γ rhythm. This input layer γ rhythm forms from the interaction of RS and FS cells, dependent on the FS cells receiving slow inhibition from deep layer SOM interneurons. In turn, granular γ rhythms drive γ rhythmicity in the superficial layers.

As in the working memory model, the circuitry of our LIP module produced a β_1 “concatenation" rhythm in the absence of input from mdPul or FEF (i.e., in the poor θ phase, Figure 3B-D). We interpreted this β_1 as a “post-excitation" rhythm, since in our model it always occurred following excitation—both that of cue presentation and that of the (prior) good θ phase. As in previous models, the excitation and the resulting plasticity were absorbed into the parameters of the model, which are set to the “post-excitation" state throughout the simulation.

As in the previous model of attention (***Lee et al., 2013***), β_2 input to deep SOM interneurons

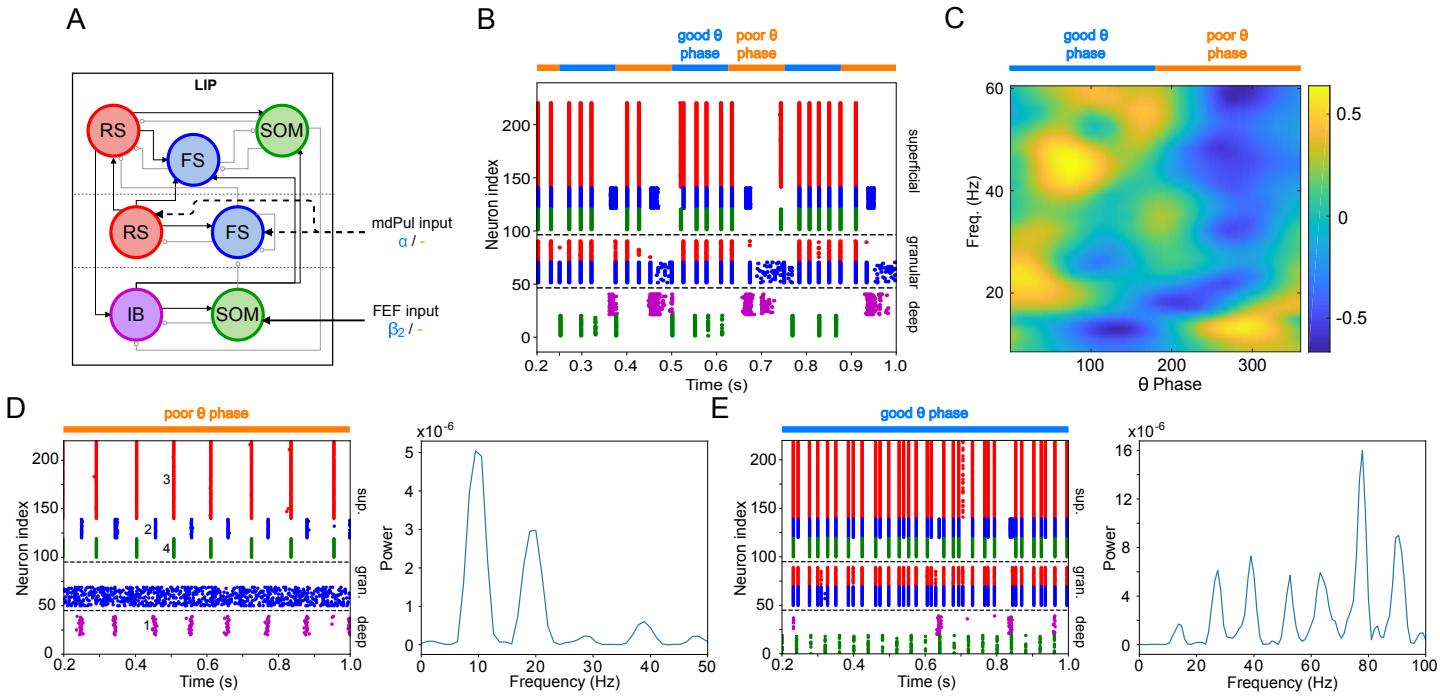

Figure 3. LIP module activity during the cue-target interval. A. Diagram of the LIP module. Symbols are as in Figure 1C. **B. LIP module spiking during a 1-second long simulation with synthetic pulvinar and FEF inputs. C. Spectral power as a function of θ phase for the LIP module.** Simulated LFP obtained from the sum of RS membrane voltages. See Methods. **D. Reproduction of LIP β_1 oscillatory rhythm, characteristic of the poor θ phase.** Left, raster plot of a 1-second simulation of LIP activity with no input, corresponding to the poor θ phase, showing a β_1 oscillatory rhythm obtained through period concatenation. A single cycle of this rhythm is labeled: 1, IB cells spike by rebound; 2, superficial FS cells spike in response to IB excitation; 3, superficial RS cells spike by rebound; 4, superficial SOM cells spike in response to RS excitation. Right, power spectrum of the LFP generated by superficial RS cells for the same simulation, with a peak in the β_1 frequency band. **E. Reproduction of LIP γ oscillatory rhythm, characteristic of the good θ phase.** Left, raster plot of a 1-second simulation of LIP activity in the presence of inputs, corresponding to the good θ phase, showing γ rhythms in the granular and superficial layers. Right, power spectrum of the LFP generated by superficial RS cells for the same simulation, with a peak in the γ frequency band.

in our LIP module partially suppressed granular FS cells, leading to disinhibition of granular RS cells. (Granular FS cells remained active, but came under the control of granular RS cells.) When this disinhibition was combined with increased excitatory input to the granular layer, a γ rhythm resulted, which then propagated to the superficial layer. During the good θ phase, the LIP module received exactly these two inputs—a β_2 input from FEF exciting deep SOM interneurons, and an α input from mdPul exciting the granular layer (Figure 3A). Thus, as in the previous model (***Lee et al., 2013***), FEF beta input to the deep layers of LIP *created* the potentiated γ in the superficial layers of LIP during the good θ phase (Figure 3B, C, & E).

The α rhythmic input that excites the RS and FS cells of the LIP module's granular layer differed from the tonic input used previously (***Lee et al., 2013***), but the result was the same. We modeled mdPul input excitation as a series of AMPA-like excitatory pulses arriving at α frequency. Since mdPul neurons are unlikely to fire in complete synchrony, the rise and decay time of the input synapses to LIP was increased (from $t_{rise} = 0.1ms$ and $t_{decay} = 0.5ms$ in AMPA synapses within the network, to $t_{rise} = 2ms$ and $t_{decay} = 10ms$ in input synapses, see Figure S4A). However, having input synapses with a shorter rise and decay time did not prevent the LIP module from generating a γ rhythm (Figure S4B), though it reduced its frequency. The γ rhythm also persisted when the rise and decay times of the input synapses were increased (Figure S4C). (We explore the range of parameters for which this mechanism produces a superficial γ more fully in Robustness and Flexibility of the LIP Module.)

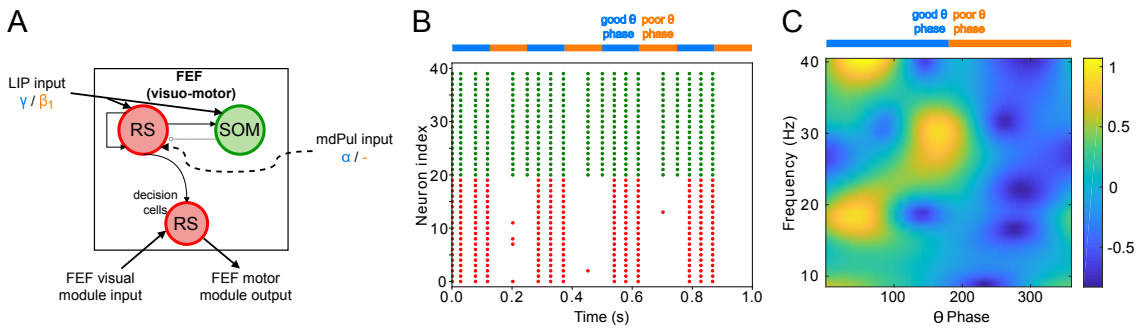

Figure 4. FEF visuo-motor cell activity during the cue-target interval. Only relevant cell types are shown. **A. Diagram of the FEF visuo-motor module.** Symbols are as in Figure 1C. **B. Raster plot of a 1s-long simulation of FEF visuo-motor cells with synthetic input.** mdPul α input during the good θ phase alters the E-I balance, enabling RS and SOM cells to form a β_2 rhythm. **C. Spectral power as a function of θ phase for the LIP module.** Simulated LFP obtained from the sum of RS membrane voltages. See Methods.

FEF Visuo-Motor Circuits Produce β_2 Oscillations When Stimulated by mdPul

The FEF visuo-motor module consisted of pyramidal regular spiking (RS) cells that were interconnected with slow interneurons (SOM cells) (Figure 4A). (The FEF visuo-motor module also included decision cells, which were only active when a target was present (see Mechanisms of Target Detection), and thus did not play a role in model behavior during the cue-target delay.) RS and SOM cells received excitatory inputs from LIP, and RS cells received excitatory inputs from mdPul. The LIP inputs arose from the LIP module in the fully connected model, and were replaced with synthetic inputs otherwise: in line with experimental data (***Fiebelkorn et al., 2019***) (and the behavior of our LIP module), LIP inputs were γ frequency during the good θ phase and β_1 frequency during the poor θ phase. As in the LIP module, mdPul inputs at α frequency arrived only during the good θ phase. Excitatory noise, representing asynchronous inputs, also arrived from mdPul during the poor θ phase.

During the poor θ phase, the excitation-inhibition (E-I) balance between SOM and RS cells was such that the SOM cells (activated by tonic excitation) silenced the RS cells. During the good θ phase, RS cells, stimulated by mdPul, fired and took control of SOM cell activity. The timescale of the inhibition generated by SOM cells determined the frequency of the rhythm resulting from RS-SOM cell interactions, a β_2. This module exhibited a motif similar to that which created a γ in LIP: when the SOM interneurons coupled to RS cells were too active, rhythms did not appear; when RS cells were stimulated, an altered E-I balance allowed rhythms (driven by RS cell firing) to emerge. Slow-decaying pulvinar stimulation (representing an input relying on a combination of NMDA and AMPA receptors) enabled up to two β_2 cycles to take place after each mdPul excitatory impulse. In the poor θ phase, the asynchronous input from pulvinar elicited a few spikes from RS cells, but this RS cell activity was not strong enough to initiate β_2 oscillations.

Figure 4B shows a raster plot of a one second-long simulation of the FEF visuo-motor cell module, with θ-rhythmic synthetic input from LIP and mdPul reproducing alternating good and poor θ phase activity. RS cells were mostly quiet during the poor θ phase, but fired and entrained SOM cells to a β_2 rhythm during the good θ phase. This β_2 rhythm was visible in the spectrogram of the simulated local field potential (LFP) for this network (Figure 4C). Section Robustness and Flexibility of the FEF Visuo-Motor Module explores the role of the inputs and of some parameters of the FEF visuo-motor module on the generated rhythms.

Mechanisms of Target Detection

FEF Visual VIP Neurons Detect Small Changes in Visual Input

The FEF visual module determined the model's response to target presentation. The appearance of a target on the screen was simulated as a transient excitatory input to FEF visual cells at a γ frequency (50Hz), presumably from an early visual area (e.g., V4, although another source, or

excitation routed through LIP, are also possible).The visual module consisted of RS, FS, VIP and SOM cells (Figures 1C & 5A). We placed this target detection network in FEF visual cells to match current knowledge of the visual attention network, but we note that similar mechanisms could be instantiated in LIP.

The heart of the target detection circuit is the VIP–SOM interaction: both of these cells receive enhanced visual input upon target presentation. VIP and SOM cells are known to mutually inhibit each other (***Tremblay et al., 2016***), but while VIP have only local connections to SOM cells, SOM cells have global connections to VIP cells (***Karnani et al., 2016***; ***Zhang et al., 2014***). This was instantiated in the module by separating the cells into two clusters, each representing a different location in visual space (Figure 5A). While SOM cells inhibited VIP cells from both clusters, VIP cells inhibited only SOM cells in the same cluster. RS and PV cells likewise connected only to other cells within the same cluster. The physiology of VIP interneurons—which exhibit large responses to relatively small inputs—also played an important role in the model dynamics.

When no target was present on screen, all SOM, RS and VIP cells in the module received input from LIP. The sizes of the inputs were such that SOM cells were active, and SOM inhibition silenced VIP and RS cells. When a target appeared, a smaller γ input (coming from early visual areas, possibly via LIP) further excited the SOM, RS and VIP cells of one cluster. Within this cluster, SOM cells, which were already highly active and exhibited a shallower f-I curve than the VIP cells (Figure S1), did not change their spiking pattern. The VIP cells in this cluster therefore received the same amount of inhibition, but a higher amount of excitation, which, due to their steeper f-I curve (Figure S1), caused them to fire. VIP firing then temporarily silenced SOM cells, disinhibiting RS cells and enabling them to fire. Though such increased excitability of RS cells could be obtained though many different mechanisms, the interaction of VIP and SOM cells amplified a small difference in excitation between two visual regions, resulting in a large RS cell response to even a small increase in excitation. We believe these mechanisms play an important role in detecting near-threshold visual stimuli, such as the low contrast target of the task we are modeling. We discuss the robustness of this module in more detail in Modeling Choices in the FEF Visual Module, and its relation to other models of VIP–SOM interactions in Discussion: Modeling Choices & Limitations.

In this module, the influence of θ rhythm phase was via the input from LIP, which was a γ rhythm in the good θ phase and a β_1 rhythm in the poor θ phase. During the good θ phase, high-frequency input and the interaction of RS and FS cells produced a burst of γ rhythmic activity in response to target appearance (Figure 5B). During the poor θ phase, single volleys of LIP input produced single volleys of FEF visual RS cell spikes (Figure 5C). Note that target detection in the FEF visual cell module is not yet adequate for a “hit" to be recorded for the model. This module’s response to a target appearing on the screen still needs to be transmitted to the FEF visuo-motor module, where a decision to act on it is made by what we call “decision cells". Only the spiking of decision cells following target appearance was considered a “hit". As will be shown in the next section, the activity of the visuo-motor module and decision cells are strongly affected by the θ rhythm.

FEF Decision Cells Enable Action Following Target Detection

The output of FEF visual and visuo-motor RS cells was transmitted to a set of RS cells in the visuo-motor module that we refer to as decision cells, whose spiking activity we interpreted as initiating action in response to target detection. These “decision cells" were modeled as simple RS pyramidal cells. Input from FEF visuo-motor cells sets the threshold of decision cell spiking, determining how likely they are to respond to (simultaneous) input from visual cells when a target appears. Decision cell spiking then sends the decision to initiate action in response to FEF motor cells (not modeled here). There is evidence to suggest that FEF motor neurons participate in overt and covert visual responses to the target; these cells can receive inputs from other brain areas, allowing them to initiate task-appropriate responses (e.g., covert attentional shifts or eye movements).

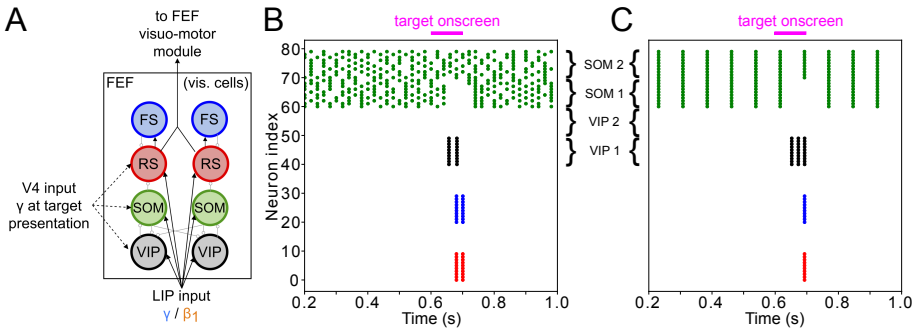

Figure 5. FEF visual module activity at target presentation. A. Diagram of the FEF visual module. Symbols are as in Figure 1C. **B. Raster plot of a 1s-long simulation of FEF visual cells with good θ phase LIP input.** A target appears on screen at $t = 600ms$ for a duration of $100ms$, producing two cycles of γ in RS and FS cells. **C. Raster plot of a 1-second simulation of FEF visual cells with poor θ phase LIP input.** A target appears on screen at $t = 600ms$ for a duration of $100ms$, producing a single volley of RS spikes.

Task Performance

Network Response to Target Appearance is Greater During the Good θ Phase

To test whether the network dynamics observed during good and poor θ phase also affect target detection, we varied the time of appearance of a simulated target (a 100ms-long train of γ frequency excitatory pulses to FEF visual neurons) across several θ cycles. The model's response to the target depended on its timing relative to the ongoing θ cycle (Figure 6). More precisely, the number of FEF decision cell spikes following target appearance was higher on average when the target appeared (i.e., when target input began) during the good θ phase (or at the transition from poor to good θ phase) compared to when it appeared during the poor θ phase (or at the transition from good to poor θ phase; Figure 6C(i)).

We translated FEF decision cell spiking into a hit rate via thresholding: we considered a trial to be a "hit" if more than half of FEF decision cells spiked at least once during the $100ms$-long window where the target was presented. In agreement with behavioral data, model hit rates varied with the cue-target interval, and followed a 4 Hz θ rhythm (Figure 6C(iii) & (iv)).

LIP→FEF Functional Connectivity Influences Network Sensitivity and Hit Rate Rhythmicity

We varied the functional connectivity from LIP to the FEF visual module by altering the strength of the chemical synapses from superficial LIP RS cells to FEF visual cells. Increasing LIP→FEF connectivity increased both hit rates (Figure 7A(i)) and false alarm rates (Figure 7A(ii)). (We considered a trial to contain a "false alarm" whenever more than half of the decision cells fired in any $25ms$-long window outside target presentation.) Computing the D' sensitivity index, which combines both hit and false alarm rates, revealed that intermediate values of LIP→FEF connectivity resulted in the highest levels of task performance (i.e., both high hit rates and low false alarm rates, Figure 7A(iii)).

Intermediate values of the conductance of LIP→FEF chemical synapses also gave rise to a temporal profile of hit rates with a dominant 8 Hz (rather than 4 Hz) component (Figure 7B). In these cases, in addition to a peak in hit rate at the beginning of the good θ phase (at 0 degrees), there was a second, smaller peak in hit rate at the beginning of the poor θ phase (Figure 7B(i) & (ii)). This was a result of LIP superficial RS spikes participating in β_1 oscillations, which excited FEF visual neurons, and rescued target detection in the poor θ phase. Plotting the number of decision cell spikes during target presentation as a function of the phase of the LIP β_1 oscillation in the poor θ phase revealed a strong influence of LIP β_1 phase on decision cell spiking for a medium but not for a low value of the LIP→FEF synaptic conductance (Figure S2A, correlation coefficient 0.33, $p < 10^{-20}$, for medium $g_{\text{LIP}\to\text{FEF}}$). The LIP→FEF synaptic conductance also influenced the dependence of the hit rate on the LIP β_1 phase (Figure S2B).

The appearance of this 8 Hz rhythm in hit rate for high LIP→FEF connectivity was also dependent on the activity of the FEF visuo-motor module, and in particular on its activity during the poor θ

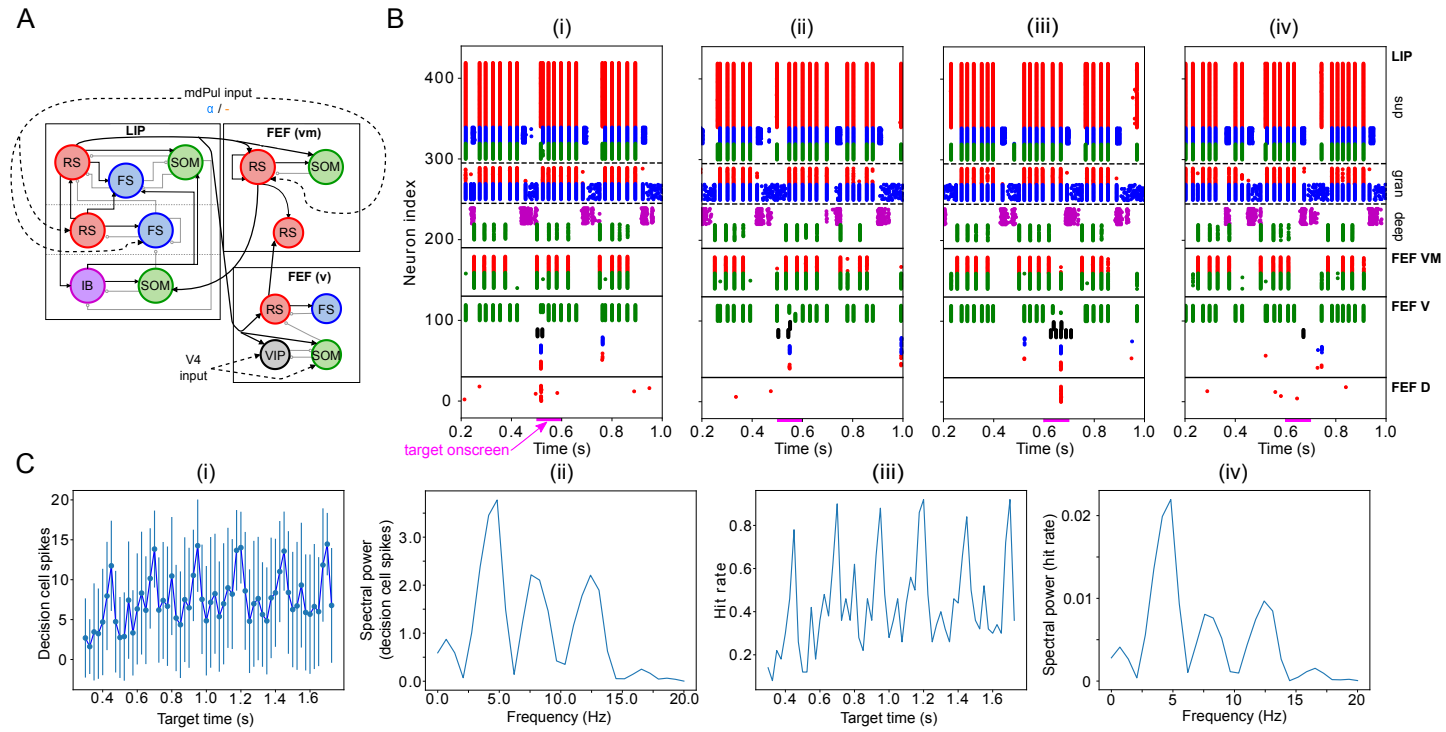

Figure 6. Model activity in response to target presentation. A. Diagram of the model. Symbols are as in Figure 1C. **B. Raster plots of the model during a 1-second long simulation with simulated mdPul input and target presentation during the good or poor θ phase.** The raster plots show activity of LIP on top, that of FEF visuo-motor cells right below, that of FEF visual cells below them, and that of FEF decision cells at the bottom. A target was presented for 100ms in the good θ phase in (i) and (ii), and in the poor θ phase in (iii) and (iv). Only in (i) and (iii) did target presentation lead to a "hit". **C. Decision cell activity and hit rate depend on θ phase.** (i) Number of decision cells spikes (with mean and standard deviation) during target appearance as a function of the cue-target interval. (ii) Power spectrum of decision cell spiking, showing a peak at a low θ frequency (4Hz). (iii) Hit rate as a function of the cue-target interval. (iv) Power spectrum of the hit rates, showing a peak at a low θ frequency (4Hz).

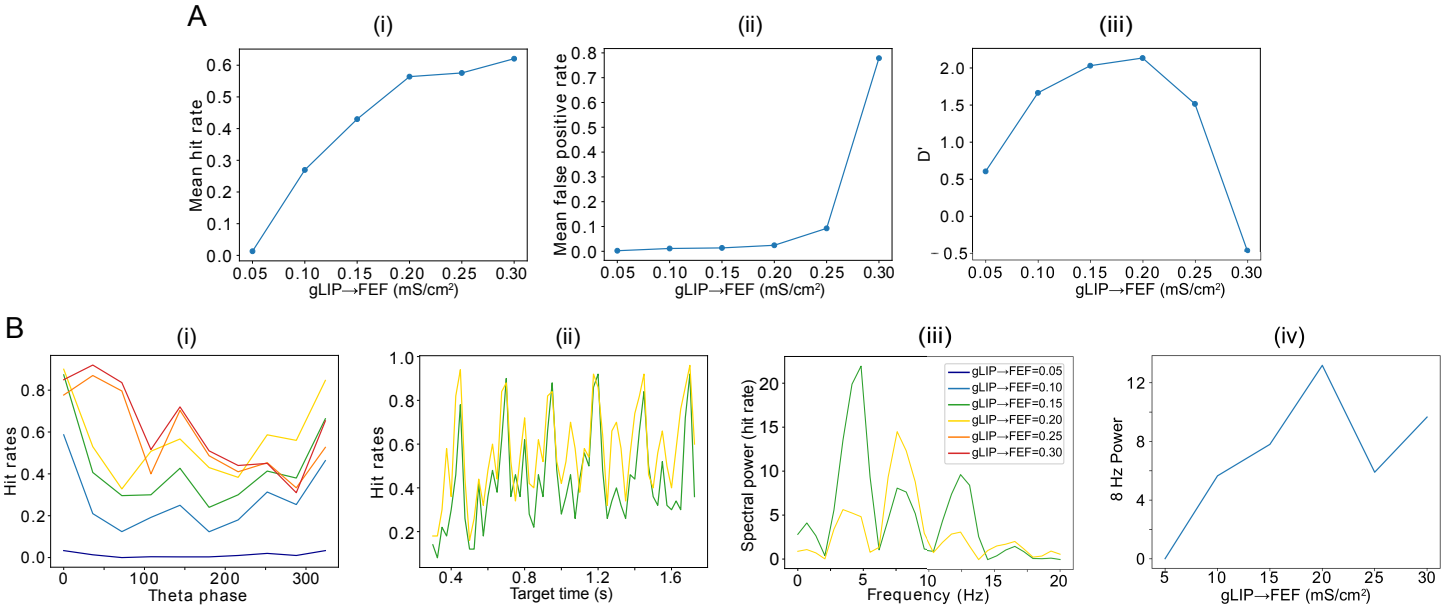

Figure 7. A. The strength of LIP→FEF chemical synapses influences network sensitivity. (i) Hit rate as a function of $g_{\text{LIP}\to\text{FEFv}}$. (ii) False alarm rate as a function of $g_{\text{LIP}\to\text{FEFv}}$. (iii) D' as a function of $g_{\text{LIP}\to\text{FEF}}$. **B. Increased $g_{\text{LIP}\to\text{FEFv}}$ leads to a stronger 8Hz component in the hit rates.** (i) Hit rate as a function of θ phase plotted for values of $g_{\text{LIP}\to\text{FEFv}}$ between 0.05 and 0.3. (ii) Hit rate as a function of the cue-target interval for $g_{\text{LIP}\to\text{FEFv}} = 0.15mS/cm^3$ and $g_{\text{LIP}\to\text{FEFv}} = 0.2mS/cm^3$. (iii) Power spectra of the hit rate time series shown in (ii). (iv) 8 Hz power as a function of $g_{\text{LIP}\to\text{FEFv}}$.

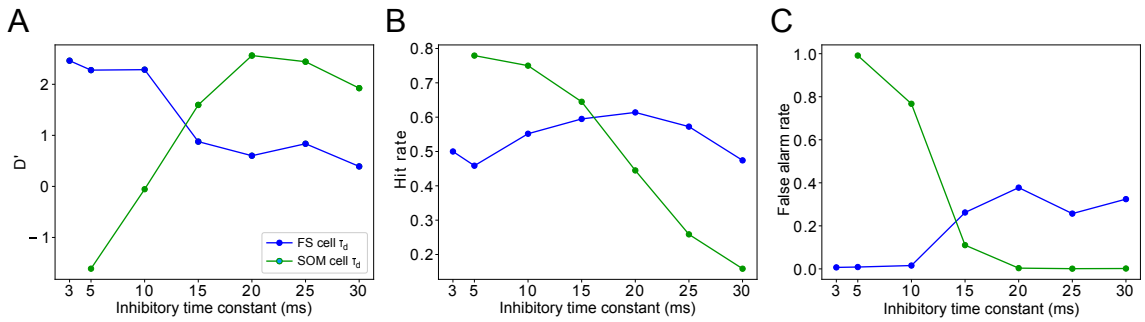

Figure 8. **Changing FEF and LIP oscillatory frequency negatively impacts task performance. A. D' measure as a function of the time constants of inhibition for SOM cells and FS cells. B. Hit rate as a function of the time constants of inhibition for SOM cells and FS cells. C. False alarm rate as a function of the time constants of inhibition for SOM cells and FS cells.**

phase. If FEF visuomotor RS cells were completely silent during the poor θ phase, decision cells were insufficiently excited to score a hit, despite high levels of input to decision cells from FEF visual cells (i.e., during target presentation with high LIP→FEF synaptic conductance; Figure S8). FEF visuo-motor module spiking during the poor θ phase depended, in turn, on sufficient noise in mdPul inputs during the poor θ phase (Figure S8), which we interpreted as asynchronous spiking in mdPul thalamocortical neurons. In sum, improved target detection during the poor θ phase (just like in the good θ phase) relied on the concomitant activity of LIP and the FEF visuo-motor module to excite FEF decision cells and bring them closer to their firing threshold.

In behavioral data (***Fiebelkorn et al., 2013***), an 8 Hz rhythm in hit rate was observed for trials in which the target and cue appeared within the same object, while a 4 Hz rhythm in hit rate was observed for trials in which the target and cue appeared within different objects. Our model thus suggests that the deployment of attention towards a cued object induces a change in functional connectivity, moderately increasing the strength of LIP→FEF connectivity, with a resulting increase in performance (as reflected by an increase in D').

Sensitivity of Target Detection is Highest for FEF Oscillations at β Frequency and LIP Oscillations at γ Frequency

One question that naturally arose from the previous results was whether the frequency of LIP and FEF rhythms is significant for task performance. To answer it, we modified the synaptic time constants of inhibition in FS cells and SOM cells ($\tau_{\text{d,FS}}$ and $\tau_{\text{d,SOM}}$, respectively) to vary the oscillatory frequencies of inhibition-paced rhythms across the β and γ ranges. We then analyzed the temporal profile of hit rates as a function of the cue-target interval, as in the previous section.

We found the sensitivity of target detection (as measured by D') was highest for $\tau_{\text{d,SOM}} \simeq 20$ ms, corresponding to observed β_2 frequencies of 25 Hz, and for $\tau_{\text{d,FS}} \leq 10$ ms, corresponding to frequencies as fast or faster than the observed 40 Hz γ rhythm (Figure 8A). The peak in sensitivity at these time constants resulted from shifts in both hit rates and false alarm rates (Figure 8B & C). We describe the mechanisms of these changes in detail below. A key point is that the activation of FEF visual module SOM cells at a γ timescale, i.e. faster than their β time constant of inhibition, provides a blanket of inhibition that prevents VIP cells from spiking outside of target presentation and reduces false alarms in the network during the good θ phase.

Effects of decreased inhibitory time constant of SOM cells: Both the hit and false alarm rates decreased monotonically as $\tau_{\text{d,SOM}}$ increased, but the false alarm rate decreased more rapidly initially and then bottomed out at nearly zero for $\tau_{\text{d,SOM}}$ around 20 ms (Figure 8A & B). As a result, $\tau_{\text{d,SOM}} < 20ms$ resulted in proportionally more false alarms, while $\tau_{\text{d,SOM}} > 20ms$ resulted in proportionally fewer hits, as compared to the highest observed sensitivity.

Because SOM cells did not exhibit self-inhibition, the rate of SOM cell firing (and the time between volleys in SOM population spiking) was controlled by the strength and rate of their input.

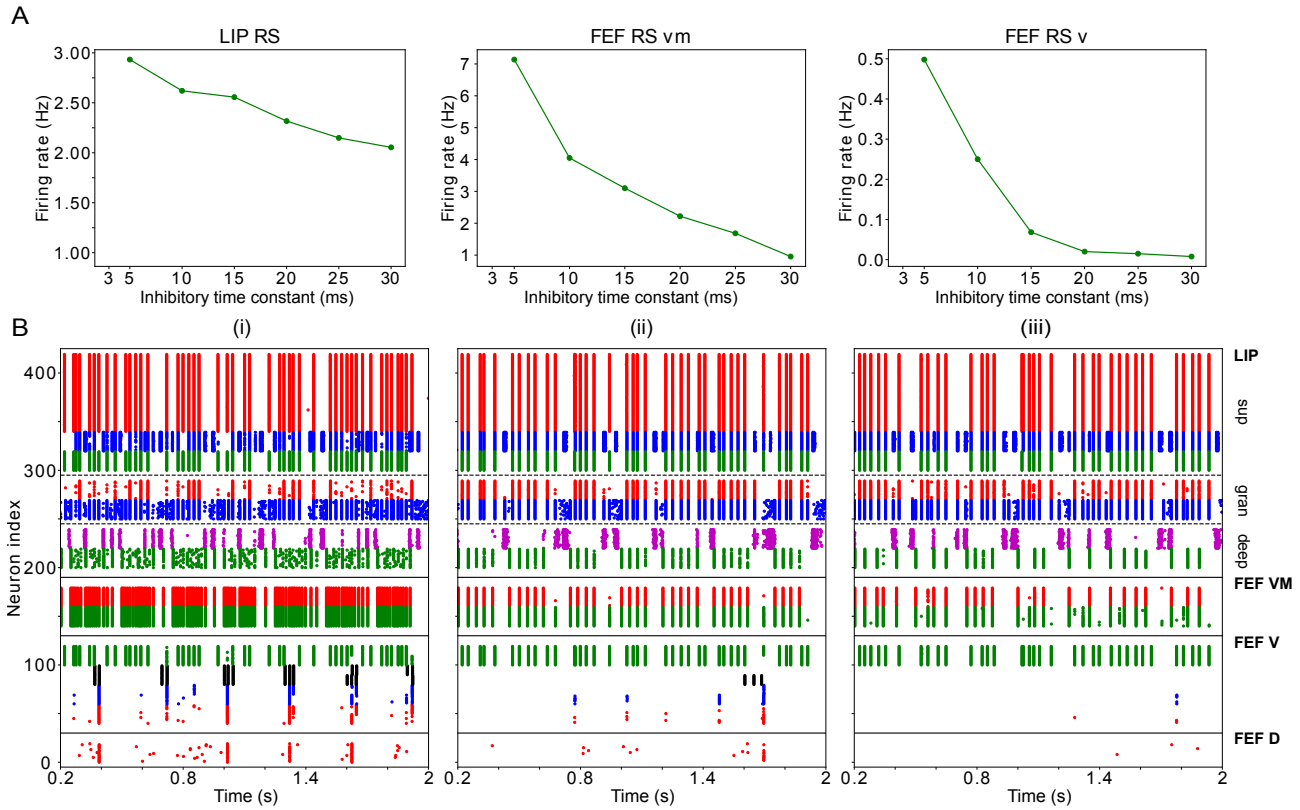

Figure 9. Changing $\tau_{d,SOM}$ impacts network dynamics and function. (A) The firing rates of RS cells in the LIP, FEF visuomotor, and FEF visual modules as a function of $\tau_{d,SOM}$. (B) Raster plots of network activity for three values of $\tau_{d,SOM}$: (i) $\tau_{d,SOM} = 5$ ms; (ii) $\tau_{d,SOM} = 20$ ms; (iii) $\tau_{d,SOM} = 25$ ms.

Whether $\tau_{d,SOM}$ was longer or shorter than the period between SOM cell volleys controlled the proportion of the time that SOM cell targets were inhibited. Thus, when $\tau_{d,SOM}$ increased, the overall firing rates of RS cells in all network modules decreased (Figure 9A), notwithstanding the complex feedback effects between LIP superficial layers and FEF visuomotor RS cells. Similarly, the activation of FEF visual module SOM cells at a timescale faster than $\tau_{d,SOM}$ was key to preventing false alarms in the network during the good θ phase, as it provided a sufficient blanket of inhibition to prevent VIP cells from spiking outside of target presentation. As $\tau_{d,SOM}$ continued to lengthen, this blanket of inhibition became stronger, and thus a stronger response from the FEF visual cells was needed to register a hit.

Thus, $\tau_{d,SOM}$ affected the decision criterion of the network—how likely the network was to register a hit in any context—with longer $\tau_{d,SOM}$ resulting in a higher decision criterion. Because target presentation was accompanied by extra input to FEF visual cells, decreasing $\tau_{d,SOM}$ from its longest value of 30 ms resulted in an increase in the hit rate even though the blanket of inhibition was still intact (Figure 9-B). Once $\tau_{d,SOM}$ fell below 20 ms, the blanket of inhibition developed "holes", and the false alarm rate began increasing (Figure 9-B). Because a false alarm could occur at any time, while a hit could only occur when a target was present, the rate of false alarms eventually increased much more quickly than the hit rate.

Effects of increased inhibitory time constant of FS cells: The hit and false alarm rates both changed non-monotonically with $\tau_{d,FS}$, and network activity depended in a more complex way on this parameter (Figure 8A & B). The hit rate decreased for $\tau_{d,FS}$ between 3 and 5 ms and above 20 ms, but increased for $\tau_{d,FS}$ between 5 and 20 ms. The false alarm rate stayed low until $\tau_{d,FS}$ reached 10 ms, and then increased rapidly until 20 ms, decreasing again at 25 ms. Despite the non-monotonicity of these curves, very low false alarm rates alongside acceptable hit rates resulted in the highest values of D' for small $\tau_{d,FS}$. More generally, the shifting balance between the hit and

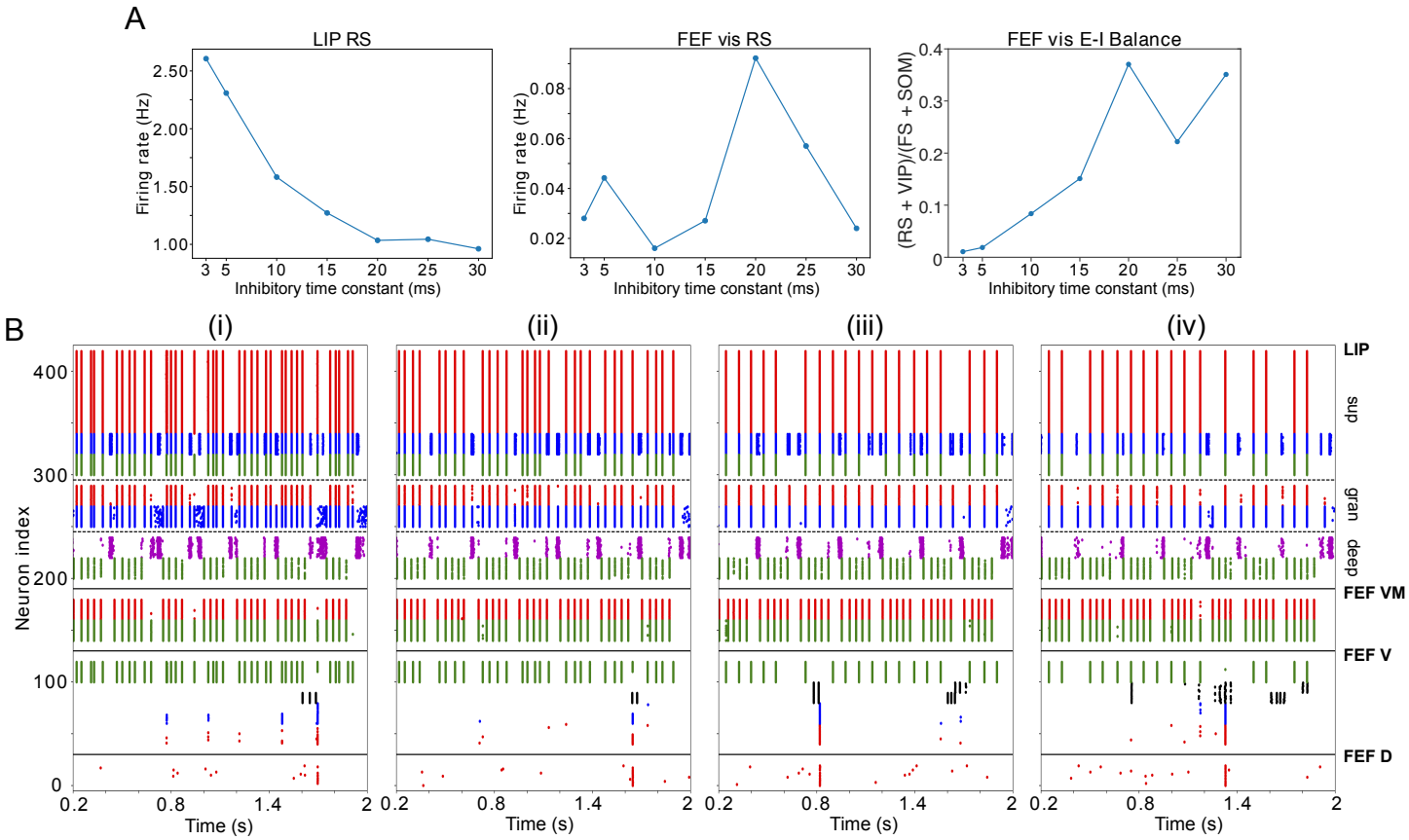

Figure 10. Changing $\tau_{d,FS}$ impacts network dynamics and function. (A) The firing rates of RS cells in the LIP superficial layer and the FEF visual module as a function of $\tau_{d,FS}$. (B) Raster plots of network activity for four values of $\tau_{d,FS}$: (i) $\tau_{d,FS} = 5$ ms (showing a hit); (ii) $\tau_{d,FS} = 10$ ms (showing a hit); (iii) $\tau_{d,SOM} = 20$ ms (showing a false alarm); (iv) $\tau_{d,FS} = 30$ ms (showing a false alarm).

false alarm rates resulted in decreasing D' as $\tau_{d,FS}$ increased (apart from a notable increase at 25 ms).

FS cells provided inhibition to RS cells in the FEF visual module and in LIP granular and superficial layers. Unlike SOM cells, FS cells exhibited self-inhibition. Thus, increasing $\tau_{d,FS}$ produced longer lasting inhibition in both FS cells and their inhibitory targets. In LIP granular and superficial layers, where the dominant inputs to RS and FS cells are the same, RS cell spiking decreased nearly monotonically with $\tau_{d,FS}$ (Figure 10A). In the FEF visual module, the situation was more complicated. The rate of FEF visual RS cell firing was controlled by $\tau_{d,FS}$ both directly, through the slowing of recurrent FS inhibition, and indirectly, through a decrease in LIP input to FEF visual VIP, SOM, and RS cells. As a result, changes in the hit and false alarm rates did not mirror changes in FEF visual RS cell activity (Figure 10A). A plot of the E-I balance (calculated as the sum of RS and VIP activity divided by the sum of FS and SOM cell activity) came closer to matching the changes in false alarm rate and sensitivity, by the logic outlined above (i.e., increases in the E-I balance leading to increases in the false alarm rate; Figure 10A). However, a full understanding of why the network sensitivity is highest for small values of $\tau_{d,FS}$ will require further work.

Model Robustness and Flexibility

As shown in the previous sections, our model reproduced both the neural dynamics and the behavioral results observed during rhythmic sampling in spatial attention (***Fiebelkorn et al., 2019***). In order to be relevant to the brain, our model must be somewhat robust to parameter changes. However, since LIP and FEF are involved in cognitive tasks other than rhythmic attention, it should also be flexible enough to allow different rhythms to appear as conditions are varied. This section

will address both these issues by looking at the conditions necessary for oscillations and target detection in the different submodules of the model.

Robustness and Flexibility of the LIP Module

The activity of the LIP module depended on both inputs from FEF and mdPul and tonic excitation to its granular layer (see Figure S6 and Influence of Tonic Excitation on LIP Behavior). While α input from mdPul helped sustain γ oscillations, it did not play as important a role as the disinhibition mediated by the (top-down) β_2 from FEF (Figure 11). When mdPul α input was absent, granular RS cells continued to spike when disinhibited by the β_2 drive to LIP deep layer SOM cells, although at a lower γ frequency ($\sim 30Hz$, Figure 11B) and at rates that sometimes failed to control granular layer FS cells in between deep SOM volleys. On the other hand, when the β_2 input to the deep layer was absent, deep SOM interneurons remained quiescent, granular layer FS cells remained tonically active, and granular layer RS cells receiving tonic FS inhibition remained quiescent. The superficial and deep layers then interacted to produce a β_1 rhythm, just as in the poor θ phase (Figure 11C). LIP rhythms also depended on the level of tonic excitation to the granular layer .

It is noteworthy that though the behavior of the LIP module was robust to some changes to the tonic excitation level, sufficient excitation produced qualitatively different dynamics in LIP with consequences the behavior of the entire network, which we hypothesized might be functional for other cognitive tasks. For example, LIP's ability to direct attention to a highly salient stimulus in a bottom-up fashion (***Bisley et al., 2011***; ***Buschman and Miller, 2007***; ***Miller and Buschman, 2013***) was reproducible in our model by supplying sufficiently strong stimulation to the LIP granular layer (presumably coming from V4), which initiated a γ rhythm even in the absence of mdPul and FEF input (Figure S6B; see Robustness and Flexibility of the FEF Visuo-Motor Module and Discussion for more details).

Robustness and Flexibility of the FEF Visuo-Motor Module

Similarly to LIP, the activity of the FEF visuo-motor module depended on rhythmic input received from LIP and mdPul, as well as on tonic excitation to its RS and SOM cells. Pulvinar input—which enabled VIP cell firing and led to RS cell disinhibition—was required for the network to achieve a β_2 rhythm during the good θ phase: without mdPul input, RS cells were quiescent in both the good and poor θ phases (Figure S7A). The frequency of mdPul input also played a role in generating sustained β_2 oscillations: input at θ or slower frequencies did not provide enough disinhibition to RS cells for them to take control of SOM cells during the entire good θ phase (Figure S7B). However, model behavior was preserved when mdPul input arrived at frequencies faster than α, and when the width of mdPul excitatory pulses was varied (Figure S7C). The frequency of the alternation of the good and poor θ phases was required to be less than half of mdPul α frequency for the network to achieve a β_2 rhythm in the good θ phase (Figure S7D).

LIP input to RS and SOM cells also influenced the activity of the FEF visuo-motor module. Simply removing this input caused RS cells to fire at a β_1 instead of a β_2 rhythm during the good θ phase, since they did not receive enough excitation to fire outside the windows of disinhibition provided by VIP spikes (Figure S5A). For the same reason, LIP input at a frequency in the α range or lower led to LIP exhibiting a β_1 rhythm in the good θ phase (Figure S5B). LIP input at β_1, β_2, or γ frequency was required to achieve the desired β_2 frequency in LIP RS cells. In particular, this meant that the FEF visuo-motor β_2 characteristic of the good θ phase could occur even if LIP was still producing the β_1 characteristic of its poor θ phase dynamics. Therefore, our model suggests that the transition from the poor to the good θ phase is likely initiated by FEF, which then recruits LIP in a top-down fashion. Increasing the frequency of LIP input above the γ range caused FEF visuo-motor RS cells to fire at a frequency faster than β_2, provided that the input was strong enough.

Even at experimentally observed frequencies, the strength of LIP input influenced FEF visuo-motor rhythms (Figure S5C). A too-weak input did not provide enough excitation for FEF to produce a β_2 rhythm during the good θ phase (it produced a β_1 rhythm instead), while with a too-strong

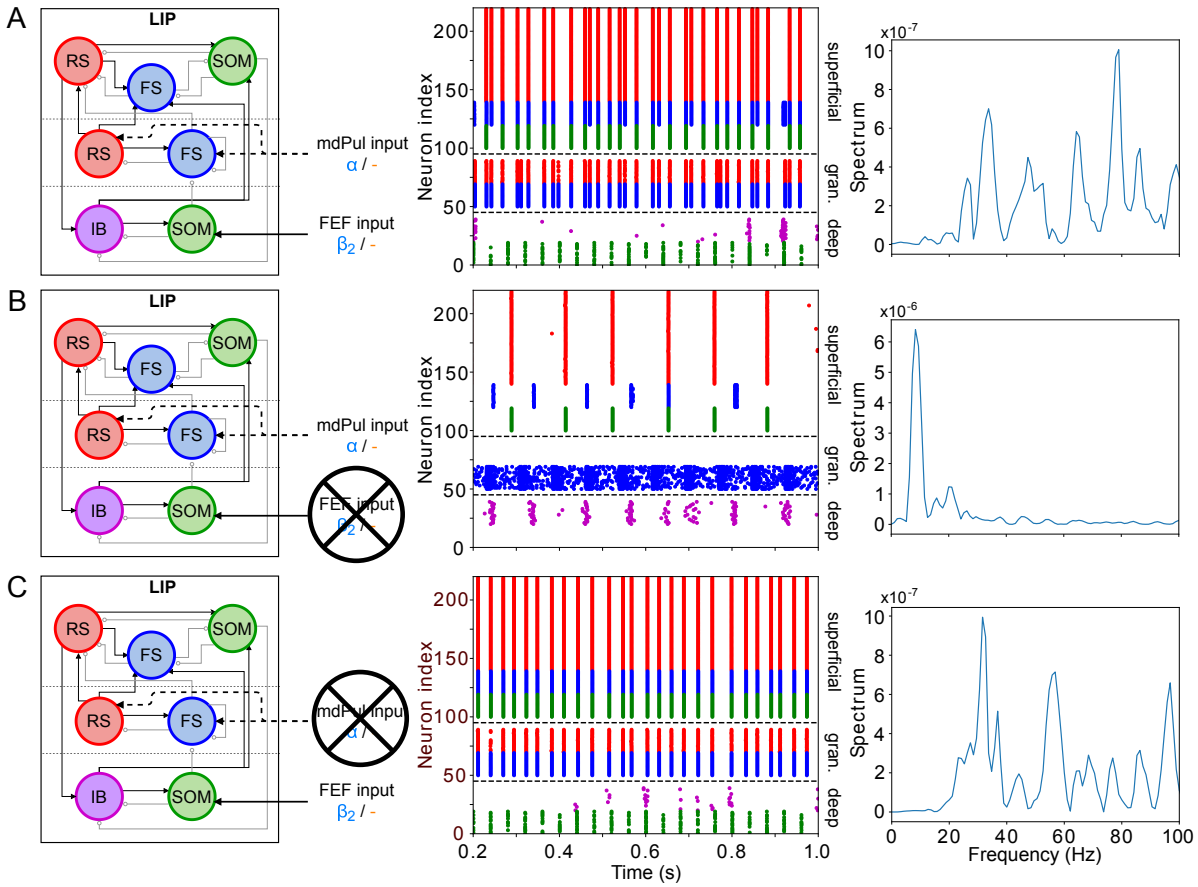

Figure 11. LIP good θ phase behavior depends on mdPul and FEF inputs. A. LIP good θ phase behavior with both mdPul and FEF inputs. B. LIP good θ phase behavior with FEF input but no mdPul input. C. LIP good θ phase behavior with mdPul input but no FEF input. Columns are as follows: Left, diagram of the model. Symbols are as in Figure 1C. Middle, raster plot of a 1s-long simulation. Right, power spectrum of the LFP generated by the network in this 1s-long simulation.

input FEF RS cell spiking followed the LIP input rhythm (at a β_1 frequency during the poor θ phase, and a γ frequency in the good θ phase). Importantly, though this behavior is undesirable for the rhythmic attention task we are modeling here, the activation of the FEF visuo-motor module by LIP input in the absence of mdPul stimulation may represent a bottom-up attentional state, in which the network responds to the appearance of a highly salient target in a bottom-up fashion.

Finally, just as LIP activity depended on the tonic excitation given to its input layer RS and FS cells, FEF visuo-motor activity depended on the tonic excitation given to its RS and SOM cells (Figure S8).

Modeling Choices in the FEF Visual Module

While simpler versions of the FEF visual module were able to detect changes in contrast, they exhibited some disadvantages that motivated our modeling choices for this module (Figure 12). A model including only RS and FS cells (Figure 12A) exhibited a γ burst during target presentation in response to strong-enough excitation of RS cells, even without the disinhibition provided by VIP cells. However, since RS cells have a larger capacitance than VIP cells, the strength of the target input had to be at least 1.5 times larger than the background stimulation from LIP to result in γ rhythmicity (Figure 12A(ii) & (iii)), which we interpreted as a high contrast target. Thus, the VIP and SOM cell circuit in the visual module played an important role in the detection of near-threshold contrast changes, and, presumably, other near-threshold stimuli.

In contrast, simulations of a model including only one interconnected network of RS, FS, VIP, and SOM cells (as opposed to two clusters of cells with different inter- and intra-cluster connectivity) were unable in our hands to satisfactorily exhibit robust target detection (Figure 12B). Robust target detection depended on VIP cells being silenced by SOM cells when no target was present, and SOM cells being silenced by VIP cells during target presentation, during both the good and the poor θ phase (that is, with background inputs from LIP in the γ or β_1 range). We were unable to achieve this behavior for any of the conductances of VIP→SOM inhibitory synapses or levels of tonic excitation to VIP and SOM cells tested. An example of an unwanted behavior in a model without clusters is shown in Figure 12B(ii) & (iii), where the inhibition from SOM to VIP was strong enough to ensure VIP cells didn't spike outside target presentation in the good θ phase (that is, when LIP input was in the γ range and SOM cells are also active at a γ rhythm), but not in the poor θ phase (when LIP input and SOM cell spiking were at β_1 frequency). Increasing the inhibition from VIP to SOM led to an inability of VIP cells to spike at target presentation. Separating SOM and VIP cells into two clusters enabled a finer tuning of the inhibition between them (for example, instead of receiving an all-or-nothing inhibition from SOM cells, VIP cells could receive inhibition from half of the SOM cells), which helped achieve the model behavior necessary for task performance under a variety of different constraints.

Discussion

We propose a biologically detailed model of LIP and FEF circuits, capable of reproducing the complex oscillatory dynamics observed in these regions during spatial attention (***Fiebelkorn et al., 2019***) in response to rhythmic pulvinar input, the presence and absence of which defined the good and poor θ phases observed experimentally during task execution (***Fiebelkorn et al., 2013***, ***2019***). The model is composed of different modules: an LIP module with a laminar structure capable of producing β_1 and γ oscillations, and motivated by previous work on memory and attention (***Kramer et al., 2008***; ***Lee et al., 2013***); and an FEF module including visual, motor, and visuomotor functional submodules, capable of producing β_2 oscillations and detecting the appearance of a target on a screen.

In this model, biophysically detailed rhythmic dynamics interact to support enhanced sensitivity in visual target detection during the good θ phase, while maintaining functional flexibility—for example, the potential for target detection during the poor θ phase. The incorporation of mechanisms

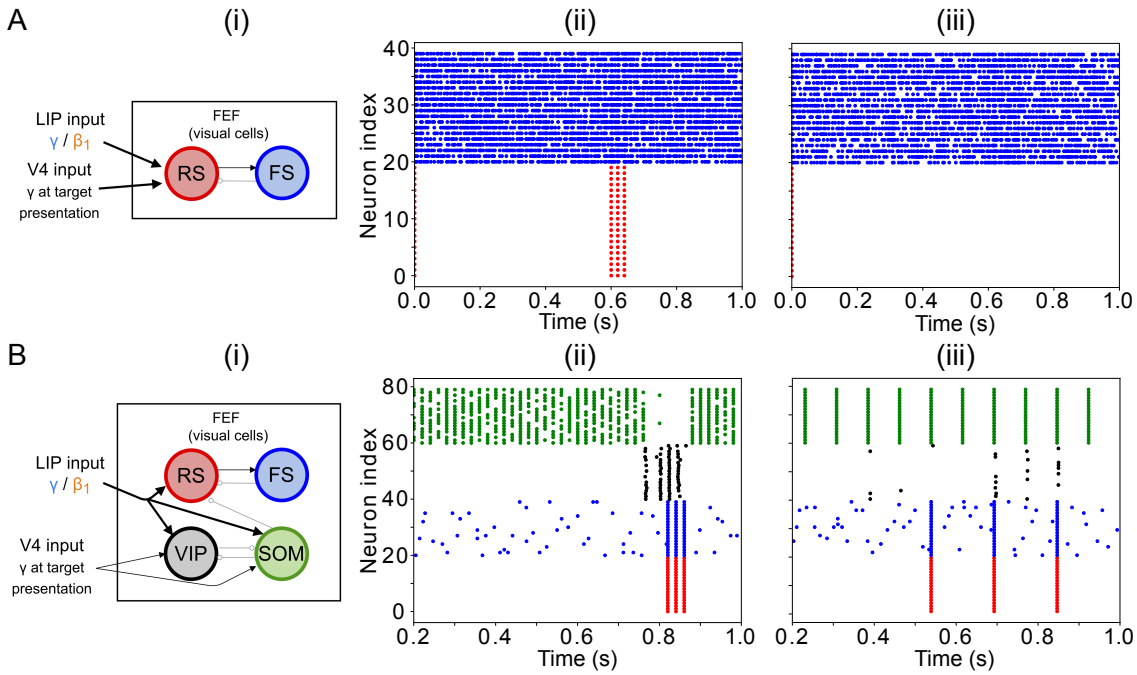

Figure 12. A. A model without VIP and SOM cells fails to detect a small change in input. (i) Diagram of FEF visual module without VIP and SOM cells. Symbols are as in Figure 1C. (ii) Raster plot of a 1-second simulation of the model with a target input applied between 600ms and 700ms at 1.5 times the strength of the background input, producing a γ burst in RS cells. (iii) Raster plot of a 1-second simulation of the model with a target input applied between 600ms and 700ms at 0.5 times the strength of the background input, producing no activity in RS cells. **B. A model with a single population leads to false alarms in the poor θ phase.** Panel (i) as above. (ii) Raster plot of a 1-second simulation of the model with good θ phase inputs, and target input applied between 600ms and 700ms, leading to γ activity in RS cells only during target presentation. (iii) Raster plot of a 1-second simulation of the model with poor θ phase inputs, and target input applied between 600ms and 700ms, leading to RS cell activity outside of target presentation.

originally developed to illuminate brain function in related but distinct cognitive contexts is a further constraint on the realism and flexibility of our model.

Our work shows that LIP→FEF functional connectivity (operationalized as the maximal synaptic conductance) can control the experimentally observed shift in hit rate periodicity from 4 Hz (for the uncued object) to 8 Hz (for the cued object). It suggests that while pulvinar primes LIP and activates FEF, it is FEF that elicits γ-rhythmic output from LIP in the context of top-down attentional control. It shows that the frequencies of observed rhythms maximize these interactions and the sensitivity of target detection, suggesting that these rhythms, rather than being epiphenomena, are key to the function of attention in the brain. Finally, our model suggests hypotheses about how multiscale rhythmic coordination may serve to sequence and segregate the activities of perceptual and motor systems. We elaborate on these points below.

LIP to FEF Connectivity Controls the Frequency of Perceptual Sensitivity

Our model replicated experimental results at the behavioral level, with hit rates that varied with the θ phase of pulvinar input to the cortex and which were increased during the good θ phase (i.e. during pulvinar stimulation). In the FEF visual module, VIP cells enabled the detection of low-contrast targets. Our work suggests that increasing the LIP→FEF functional connectivity (by increasing the conductance of LIP chemical synapses onto FEF visual cells) increases first hit rates and then false alarm rates, so that intermediate values of connection strength lead to peak sensitivity of target detection. These intermediate values of LIP→FEF visual module connectivity are also associated with a strong 8Hz θ component in the hit rates, which has been associated experimentally with attention towards a cued object (***Fiebelkorn et al., 2013***).

Our model thus suggests that the appearance of a cue on the screen might enhance LIP→FEF visual cell functional connectivity, leading to increased perceptual sensitivity especially during the

poor θ phase and an 8 Hz dominant frequency in the hit rate spectrum. In other words, the 8 Hz hit rates in our model did not come from the division of a 4 Hz rhythm into multiple possible target locations, as previously suggested for similar data (***Landau and Fries, 2012***), but were a consequence of the increased LIP→FEF connection strength for the cued object. In our results, very strong LIP→FEF connectivity led to high false alarm rates, and such excessive connectivity may be linked to hallucinations (as in the detection of a target in the absence of a visual stimulus) or other pathologies in visual perception.

In this work, the increase in LIP→FEF functional connectivity is implemented via an increase in the maximal conductance of the chemical synapses from LIP to FEF. However, there are multiple ways such an increase in drive could arise. For example, either FEF or LIP may be disinhibited by the activation of VIP interneurons in these regions, or thalamus may modulate the gain of LIP→FEF connectivity via a cortico-thalamo-cortical feedforward pathway, as described in the next section. Multiple mechanisms may be implemented in the brain, to allow multiple information streams—e.g. reward statistics from superior colliculus or learned associations from hippocampus or amygdala—to influence the attentional processing of a given visual location.

Interacting Rhythms in FEF and LIP Mediate the Competition Between Top-Down and Bottom-Up Control of Visual Attention

The rhythms in our network did not operate independently, but interacted with one another to give rise to the observed neural activity and behavior. The FEF visuomotor β_2 rhythm was necessary for the production of LIP γ, at least in the context of our task (in which the LIP granular layers did not receive very strong inputs). This β_2 oscillation—activated by pulvinar excitation of FEF visuomotor cells in the good θ phase—elicited γ oscillations from LIP by effectively disinhibiting LIP granular layer pyramidal cells. LIP γ oscillations acted to enhance sensory processing in the network by stimulating FEF visual cells, making them more likely to detect a target. This increased hit rates during the good θ phase, as did the direct excitation of decision cells by FEF visuomotor β_2 rhythms. Thus, our results suggest that the FEF visuomotor module *leads* the rhythmic attention process in a top-down manner, and our model makes the prediction that the good θ phase is associated with the appearance of β_2 oscillations in FEF *before* γ oscillations in LIP.

Under different stimulation parameters, our model is also able to generate LIP γ oscillations without FEF β_2 input, provided that the tonic excitation to the LIP granular layers is strong enough. In particular, this means that a very salient stimulus, by providing strong excitation to the LIP input layers, could lead to enhanced sensory processing in a bottom-up fashion. FEF visuomotor cells are able to produce a β_1, a β_2 or a γ depending on the strength of inputs from LIP; thus, FEF could participate in different (frequency-specific) functional networks depending on whether visuomotor circuits are activated by highly salient as opposed to near-threshold stimuli.

An important recent rate-based computational model (***Jaramillo et al., 2019***) suggests that pulvinar functions by modulating the gain of feedforward (FF) cortico-cortical connectivity and by altering the balance between feedforward and feedback (FB) cortico-thalamo-cortical (CTC) pathways. This work draws on the fact that the pulvinar interacts with the cortex via two pathways: in addition to feedback pathways in which projections return to the deep layers of the cortical area from which input arrives, pulvinar participates in feedforward pathways in which cortical input originating in one area (A) activates projections to the granular layers of a different cortical area (B), “boosting" the direct connections from area A to area B. In this previous model, it is the latter cortico-thalamo-cortical (CTC) feedforward pathway through which pulvinar excitability (which is fixed for the duration of a trial) changes the strength of cortico-cortical connectivity (***Jaramillo et al., 2019***).

In our model, the gain of feedforward connectivity (as indexed by the conductance of synapses from LIP→FEF) plays a similar role in tuning the network’s sensitivity for target detection, representing the difference between cued and uncued locations. However, the mechanisms by which pulvinar affects the dynamics of LIP and FEF are quite different. The current work admits an

interpretation in which both LIP and FEF are the targets of FF CTC pathways, potentially originating in lower-level visual areas, such as V4. Furthermore, pulvinar input has its own temporal dynamics, and pulvinar input induces disparate dynamical responses in FEF and LIP, helping to create a β_2 rhythm in FEF and a γ rhythm in LIP during the good θ phase. We suggest that these dynamic changes, rather than biasing a competition between FF and FB information transmission, allow the pulvinar to increase the precision of both FF and FB information transmission between FEF and LIP, effectively optimizing the sensitivity of the network to target appearance during the good θ phase. This increase in the precision of information transmission is due to the deployment of different rhythmic dynamics in the good and poor θ phases: in the good θ phase, an FEF β_2 mediates top-down information transmission as well as lowering the threshold for and changing the temporal dynamics of target detection, while an LIP γ mediates bottom-up information transmission; in the poor θ phase, information transmission between FEF and LIP (i.e., spiking in FEF deep layers and LIP superficial layers) occurs at α frequency (which also changes the threshold and temporal dynamics of target detection in FEF). Altering the frequencies of either the FEF β_2 or the LIP γ decreases the sensitivity of the network. Thus, the dynamics revealed by our model are more complex and more finely tuned to the task at hand than those discussed in the previous model.

This prior work also addressed how pulvinar activity could alter rhythmicity in cortex. In that work, V4 rhythms at lamina-specific frequencies were modeled via E-I networks with lamina-dependent timescales of inhibition, giving rise to a superficial γ and a deep α. Feedback connections arising from the thalamus target interneurons in deep layers (***Cruikshank et al., 2010***; ***Zhou et al., 2018***; ***Audette et al., 2018***). Thus, in this previous work, pulvinar feedback pathways inhibit deep layer excitatory cells, resulting in less α; and the disinhibition of deep layer E-I networks explains experimental observations that pulvinar lesion results in an increase in α rhythmicity in V4 (***Zhou et al., 2016***). In contrast, in our model, it is top-down β from FEF that disrupts LIP α/β_1, even though pulvinar input to LIP granular layers also contributes to the disruption of LIP's concatenation β_1 rhythm. Our model suggests that pulvinar lesion might indirectly increase low-frequency (β_1) power in LIP, just as it increases α power in V4, although through a different mechanism.

Timescales of Observed Rhythms Optimize Task Performance

The frequency of FEF and LIP oscillations in our model has consequences for task performance, and the values typically reported in experiments in fact produce peak levels of sensitivity in our attention network. More precisely, increasing the oscillatory frequency of FEF visuomotor cells from β_2 to γ or reducing LIP oscillatory frequency during the good θ phase from γ to β_2, by changing the time constants of local inhibition, led to higher false alarm rates, with little to no benefit on hit rates.

The optimization of network sensitivity by FEF β_2 and LIP γ results from the way that these rhythms and their interactions subtly and differentially alter the excitation/inhibition balance in different layers and populations of LIP and FEF during different phases of the θ rhythm (see Task Performance). These observations point to one important role of rhythms in mediating the effects of attention. However, an account of the effects of rhythms in terms of the E/I balance of FEF and LIP neuronal populations is incomplete, as it omits the temporal dynamics of both neural activity and its behavioral consequences. In both experimental data (***Fiebelkorn et al., 2013***, ***2019***) and our model, hit rate (and false alarm rate) varied not only between "conditions" (i.e., cued vs. uncued object/LIP→FEF connectivity, time scale of inhibition/rhythmic frequency), but also in time. The phase of θ, FEF β_2, LIP γ, and pulvinar α all have an effect on target detection (and its sensitivity).

We suggest that these temporal dynamics of network activity are not coincidental or epiphenomenological, but play important functional roles. The first of these is to synchronize and sequence precise monitoring and information transmission with (multiple) other computational processes occurring in other brain regions, each of which may have a different characteristic frequency (for example, β_2 for motor processes, and γ for visual processes). The second is to provide periodic windows of enhanced sensitivity, that enable precise monitoring of a given region of the visual field with acceptable temporal "coverage", while also minimizing energetic cost and allowing monitoring

to be interleaved with other computational imperatives, including monitoring of other regions and motor planning and execution. We further elaborate on this sequencing and segregation of cognitive functions below.

Rhythmic Sampling and Turn-Taking Between Sensory, Cognitive, and Motor Networks

As the good θ phase is associated with improved sensory perception and behavioral performance in attention tasks (***Fiebelkorn and Kastner, 2019b***), one could wonder what need is served by the poor θ phase—and, indeed, the θ rhythm itself—in the first place.

One possibility is that the θ rhythm is a solution to the necessity of attending to multiple objects “at once", allowing the focus of attention to switch between objects θ-rhythmically. In this account, the poor θ phase for the representation of one object or location would occur simultaneously with the good θ phase for the representation of another object or location (***Fiebelkorn et al., 2013***; ***Landau and Fries, 2012***). In our model, this could be achieved with multiple copies of LIP and FEF representing one cortical columnar network for each object to be monitored; pulvinar inputs would select the attended object at any point in time, and manage switching the attentional focus. Even when attention is deployed at a single location, the break in attentional focus allowed by the poor θ phase would allow attention and behavior to adapt quickly to changes in visual stimuli and their perceived salience. In this framework, the good θ phase could be described as a sampling phase for one location, while the poor θ phase could be described as an exploration phase (***Fiebelkorn and Kastner, 2019b***).

Alternatively, it has been hypothesized that the poor θ phase could enable the planning and execution of motor actions (***Fiebelkorn and Kastner, 2019b***). These different accounts of the role of the θ rhythm in perceptual sensitivity are not incompatible: the θ rhythm may be a mechanism that *interleaves* periodic attention to multiple objects or locations with motor execution, with movements occurring at the transitions between good and poor θ phases, each of which represents attention to one of several stimuli. Essentially, movement would be one more attentional focus, sequenced in turn with multiple salient regions of the visual field.

A deeper understanding of the role of the θ rhythm awaits a detailed investigation of pulvinar activity and the mechanisms of θ rhythmicity and spatial selection in this task. In ongoing work, we are extending the current model to explore how circuits in the pulvinar and the superior colliculus may coordinate ongoing periodic temporal dynamics, as modeled here, among multiple identical networks representing different spatial locations and/or objects.

Modeling Choices & Limitations

As described in the Introduction, our model represents a number of simplifications relative to the full dynamics of the visual attention network in the context of this task. The model presented here is intended to allow realistic insights into the mechanisms underlying observed brain dynamics and their functional consequences while avoiding excessive complexity. Thus, we have chosen to highlight the cell types and connections necessary to produce the dynamics of interest, while leaving out other cell types and connections. In particular, the spatial structure of the full Egly-Driver task is beyond the scope of the current model. The full task involves spatially informative cues activating subpopulations that respond selectively to spatial locations and/or objects. This greater mechanistic complexity, in addition to involving a detailed pulvinar model and inputs from other regions, may also involve cell types and connections omitted in the current model, for example VIP cells and excitatory connections between RS cells in LIP superficial layers. VIP cells may participate, e.g., by mediating the disinhibition of spatially selective populations. Excitatory synapses among cortical pyramidal cells, which are extremely important for plasticity and formation of cell assemblies, may also be important in the selection of spatially specific subpopulations. But our work shows that neither are necessary for the current model (a stepping stone to a more complex model of the full Egly-Driver task), in which all the cells in LIP can be thought of as part of a single, cue-relevant

cell assembly (although dividing FEF visual neurons into two populations was necessary for the detection of low-contrast targets).

We have also chosen to model relatively small networks of biophysically detailed neurons. In order for the behavior of small networks to qualitatively match the dynamics of much larger networks, their model parameters often must be different from those of the larger networks. Their dynamics also may be different, in ways that we believe are irrelevant to understanding the qualitative dynamics of the network and the functional implications of interest—for example, rhythms that are more regular than those seen *in vivo*. Testing the conclusions of models such as ours in larger, more detailed models, as well as in experiments, is essential. However, initial modeling studies in smaller, simplified networks are indispensable in generating initial hypotheses about the mechanisms and functions of brain dynamics.

The parameters of our model are determined in part by the use of model components that have qualitatively reproduced brain dynamics relevant to other physiological and cognitive contexts: a model of cholinergic attentional modulation in laminar cortex (***Lee et al., 2013***), and models of interlaminar interactions in parietal cortex that instantiate a working memory mechanism (***Kramer et al., 2008***; ***Gelastopoulos et al., 2019***). The use of these components places an additional constraint on model parameters, which are otherwise derived from experimental data in rodents. The differences between rodent and primate neocortex are numerous. Relative to rodents, primates have a 50% greater proportion of interneurons, due in large part to an increase in calretinin, VIP, and neurogliaform interneurons in the superficial layers of association cortex, which distinguishes association and sensory cortices in primates but not rodents (***Džaja et al., 2014***; ***Krienen et al., 2020***; ***Hodge et al., 2019***). Gene expression patterns of interneuron subtypes also differ more between cortical regions in primates than rodents, suggesting that interneurons may be more specifically tailored to different cortical regions in primates (***Krienen et al., 2020***).

Among these many differences between rodents and primates, there are a few that particularly influence the dynamics of our model. The increase in superficial VIP cells in primates suggests these interneurons are likely part of the circuitry of LIP superficial layers, despite their absence in our model. As discussed above, VIP cells may play a role in determining the allocation of attention between objects in the full Egly-Driver task. However, our results suggest they do not qualitatively alter the dynamics following cue presentation; in our hands, placing a target-detection circuit in LIP supeficial layers—like the one modeled in the FEF visual module—did not alter LIP rhythms or improve detection of low-contrast targets. In monkeys relative to rats, PV-positive basket cells have been shown to have a higher input resistance and a lower firing threshold and thus to be more excitable (***Povysheva et al., 2008***). In rats, PV-positive basket cells fired in response to stimulation with a substantial delay, and generated spike trains interrupted by quiescent periods (***Povysheva et al., 2008***), hallmarks of stuttering interneurons exhibiting a D-current (***Golomb et al., 2007***). Although originally parametrized using data from rat hippocampus, our model FS cells lack a D-current, and thus exhibit behavior more similar to primate than to rodent FS cells. Another between-species difference with potential consequences for dynamics in the present model is that supragranular pyramidal neurons are known to exhibit a higher h-current conductance in humans as compared to mice (***Kalmbach et al., 2018***). This higher h-current conductance was shown to promote transfer of θ frequencies from the dendrites to the soma of human pyramidal neurons (***Kalmbach et al., 2018***). In our model, a higher h-current conductance in superficial pyramidal cells might thus lead to a stronger θ resonance in these cells.

We have chosen to model FEF and LIP as driven θ-rhythmically by simulated mdPul input. As we mention in the Introduction, this is consistent with experimental observations that mdPul exerts a Granger causal influence over FEF and LIP at α frequency only during the good θ phase (***Fiebelkorn et al., 2013***, ***2019***). This Granger causal influence means that the α rhythms in FEF and LIP are statistically dependent on the α rhythm in mdPul, such that, e.g., changes in the phase or frequency of FEF and LIP α are predicted by changes in mdPul α. This α-frequency drive during the good θ phase also amounts to a θ-rhythmic drive from mdPul to FEF and LIP, which is

sufficient—in our model—to induce the experimentally observed θ rhythmicity in the dynamics and function of LIP and FEF. However, we cannot rule out the possibility that FEF and LIP also exhibit θ rhythmicity or resonance, or that they (and/or the pulvinar) are paced by θ-rhythmic drive from one or more other brain regions. Indeed, neocortical SOM interneurons have been shown to form electrically coupled networks that generate oscillations at θ frequencies (***Beierlein et al., 2000***; ***Fanselow et al., 2008***; ***Hu and Agmon, 2015***; ***Huang et al., 2020***). These oscillations occur in response to persistent activation by synaptic inputs, metabotropic glutamate agonism, and muscarinic acetylcholine agonism (***Beierlein et al., 2000***; ***Fanselow et al., 2008***) as well as in response to salient visual stimuli (***Huang et al., 2020***), and exert a coherent inhibitory influence on cortical pyramidal cells and FS interneurons (***Beierlein et al., 2000***; ***Karnani et al., 2016***; ***Safari et al., 2017***). Coupled with a potential θ resonance in superficial RS cells induced by increased levels of h-current in humans (see above), such a θ-rhythmic SOM network could result in endogenous θ rhythmicity in LIP superficial layers. Whether and how this θ rhythmicity would change our results is an important question for future investigations.

Finally, in our FEF visual module, the interactions of inhibitory PV, SOM, and VIP interneurons within and across cortical columns produce a circuit that is particularly sensitive to low-contrast stimuli modeled as a weak input to one column and not another. The functional role of interactions between these three interneuron types has received considerable attention (***Karnani et al., 2016***; ***Yang et al., 2016***; ***Lee et al., 2017***; ***Dipoppa et al., 2018***; ***Krabbe et al., 2019***; ***Lee et al., 2019***; ***Garrett et al., 2020***; ***Hertäg and Sprekeler, 2020***; ***Keller et al., 2020***; ***Millman et al., 2020***; ***Veit et al., 2021***). This literature highlights the role of VIP interneurons in disinhibiting pyramidal cells (via inhibition of SOM cells) to produce context-dependent stimulus sensitivity. VIP-mediated disinhibition has been implicated in (i) detection of stimulus and surround differences (***Keller et al., 2020***), (ii) the creation of a high gain regime that increases sensitivity to weak inputs (***Millman et al., 2020***), (iii) the desynchronization of gamma oscillations representing spatially discontiguous visual features (***Veit et al., 2021***), (iv) the facilitation of auditory cortical stimulus responses by nicotinic acetylcholine receptor activation (***Askew et al., 2019***), (v) response reversal (***Del Molino et al., 2017***), (vi) the coding of prediction errors (***Hertäg and Sprekeler, 2020***), and (vii) the gating of information flow between cortical regions (***Yang et al., 2016***; ***Lee et al., 2017***; ***Krabbe et al., 2019***; ***Lee et al., 2019***). These results motivate in part the circuitry of the FEF visual module in the present model. A number of other models have been constructed to explore these effects, including rate models (***Millman et al., 2020***; ***Dipoppa et al., 2018***; ***Hertäg and Sprekeler, 2020***), mean-field models (***Veit et al., 2021***), and spiking models (***Yang et al., 2016***; ***Lee et al., 2017***; ***Del Molino et al., 2017***; ***Veit et al., 2021***). While a full understanding of the relationships between these models is beyond the scope of the current work, in our model, both pyramidal disinhibition via VIP-mediated SOM suppression and intercolumnar inhibition via SOM cells were required for the amplification of small inputs. The latter feature is not common in existing models of VIP-SOM interactions (but see ***Veit et al.*** (***2021***)). Another requirement is that our VIP interneurons exhibit a steeper f-I curve than our SOM interneurons (Figure S1). VIP interneurons are among the interneurons with the highest input resistance and are therefore among the most excitable (***Rudy et al., 2011***), and cortical and thalamic inputs are greatest onto VIP interneurons as opposed to PV or SOM cells (***Wall et al., 2016***). Our model is thus in line with recent investigations suggesting that a stabilized supralinear network with three interneuron types having a distribution of f-I curves can mediate an input-strength dependent switch between a (VIP-mediated) high gain regime that increases sensitivity to weak inputs and a (SOM-mediated) low gain regime that stabilizes the network response to strong inputs (***Millman et al., 2020***). Such disinhibitory mechanisms are clearly widespread in the cortex and an important subject for future work.

Channel	$g\ (mS/cm^2)$	$E\ (mV)$	p	q	τ_m (ms)	m_∞	τ_h (ms)	h_∞
L	1	-70	0	0	-	-	-	-
Na	200	50	3	1	-	$\frac{1}{1+e^{\frac{-V-34.5}{10}}}$	$0.15+\frac{1.15}{1+e^{\frac{V+33.5}{15}}}$	$\frac{1}{1+e^{\frac{V+59.4}{10.7}}}$
K	20	-95	4	0	$0.25+4.35\cdot e^{-\frac{\lvert V+10\rvert}{10}}$	$\frac{1}{1+e^{\frac{-V-29.5}{10}}}$	-	-
h	25	-35	1	0	$\frac{1}{e^{-14.6-0.086V}+e^{-1.87+0.07V}}$	$\frac{1}{1+e^{\frac{V+87.5}{5.5}}}$	-	-

Table 1. Ion channel parameters for RS cells

Channel	$g\ (mS/cm^2)$	$E\ (mV)$	p	q	τ_m	m_∞	τ_h	h_∞
L	1	-65	0	0	-	-	-	-
Na	200	50	3	1	-	$\frac{1}{1+e^{\frac{-V-38}{10}}}$	$0.225+\frac{1.125}{1+e^{\frac{V+37}{15}}}$	$\frac{1}{1+e^{\frac{V+58.3}{6.7}}}$
K	20	-100	4	0	$0.25+4.35e^{-\frac{\lvert V+10\rvert}{10}}$	$\frac{1}{1+e^{\frac{-V-27}{11.5}}}$	-	-

Table 2. Ion channel parameters for FS cells

Methods

Equations Governing Model Neurons

The model presented in this article was adapted from ***Kramer et al.*** (***2008***) and ***Gelastopoulos et al.*** (***2019***). These laminar models reproduce somatosensory and parietal rhythmic dynamics, and the cells are reductions of detailed multi-compartment representations of rat cortical neurons (***Traub et al., 2005***). The current model consisted of Hodgkin-Huxley neurons, modeled with a single compartment except for LIP intrinsically bursting (IB) cells which were modeled with four compartments. The membrane potential V of each single-compartment neuron and each IB cell compartment followed an equation of the form:

$$C\frac{dV}{dt} = -\sum I_{\text{m}} - \sum I_{\text{syn}} - I_{\text{ran}}$$

where C is the membrane capacitance, I_{m} are the membrane currents, I_{syn} are the synaptic currents, and I_{ran} is a random input current. Some cells are also electrically coupled with gap junctions. The membrane capacitance was equal to $0.9\mu F/cm^2$ for all neurons except VIP interneurons, for which it was $2\mu F/cm^2$

Our regular spiking (RS) pyramidal cell model included a leak current I_{L}, a sodium current I_{Na}, a potassium current I_{K}, and a hyperpolarization activated current (h-current) I_{AR}. The conductances of these currents (Table 1) were adapted in ***Traub et al.*** (***2005***) from experiments on rat hippocampal neurons (***Martina and Jonas, 1997***). There were 80 RS cells in our LIP superficial layer model, 20 in LIP granular layer, 20 in visuo-motor FEF, and 20 in visual FEF. The 20 decision cells in visuo-motor FEF were also RS cells.

Our fast spiking (FS) interneuron model in LIP and FEF included a leak current I_{L}, a sodium current I_{Na}, and a potassium current I_{K}. The conductances of these currents (Table 2) were adapted

Channel	$g\ (mS/cm^2)$	$E\ (mV)$	p	q	τ_m	m_∞	τ_h	h_∞
L	6	-65	0	0	-	-	-	-
Na	200	50	3	1	-	$\frac{1}{1+e^{\frac{-V-38}{10}}}$	$0.225+\frac{1.125}{1+e^{\frac{V+37}{15}}}$	$\frac{1}{1+e^{\frac{V+58.3}{6.7}}}$
K	10	-100	4	0	$0.25+4.35\cdot e^{-\frac{\lvert V+10\rvert}{10}}$	$\frac{1}{1+e^{\frac{-V-27}{11.5}}}$	-	-
h	50	-35	1	0	$\frac{1}{e^{-14.6-0.086V}+e^{-1.87+0.07V}}$	$\frac{1}{1+e^{\frac{V+75*mV}{5.5}}}$	-	-

Table 3. Ion channel parameters for SOM cells

Channel	$g\ (mS/cm^2)$	$E\ (mV)$	p	q	τ_m	m_∞	τ_h	h_∞
L	0.25	-70	0	0	-	-	-	-
Na	112.5	50	3	1	-	$\frac{1}{1+e^{-\frac{V+24}{11.5}}}$	$0.5+\frac{14}{1+e^{\frac{V+60}{12}}}$	$\frac{1}{1+e^{\frac{V+58.3}{6.7}}}$
K	225	-90	2	0	$\left(0.087+\frac{11.4}{1+e^{\frac{V+14.6}{8.6}}}\right)\cdot\left(0.087+\frac{11.4}{1+e^{-\frac{V-1.3}{18.7}}}\right)$	$\frac{1}{1+e^{-\frac{V+12.4}{6.8}}}$	-	-
D	4	-90	3	1	2	$\frac{1}{1+e^{-\frac{V+50}{20}}}$	150	$\frac{1}{1+e^{\frac{V+70}{6}}}$

Table 4. Ion channel parameters for VIP cells

Channel	$g\ (mS/cm^2)$	$E\ (mV)$	p	q	τ_m	m_∞	τ_h	h_∞
L	2 (a.d., b.d.) 1 (soma) 0.25 (axon)	-70	0	0	-	-	-	-
Na	125 (a.d., b.d.) 50 (soma) 100 (axon)	50	3	1	-	$\frac{1}{1+e^{\frac{-V-34.5}{10}}}$	$0.15+\frac{1.15}{1+e^{\frac{V+33.5}{15}}}$	$\frac{1}{1+e^{\frac{V+59.4}{10.7}}}$
K	10 (a.d., b.d., soma) 5 (axon)	-95	4	0	$0.25+4.35\cdot e^{-\frac{\lvert V+10\rvert}{10}}$	$\frac{1}{1+e^{\frac{-V-29.5}{10}}}$	-	-
h	155 (a.d.) 115 (b.d)	-25	1	0	$\frac{1}{e^{-14.6-0.086V}+e^{-1.87+0.07V}}$	$\frac{1}{1+e^{\frac{V+75}{5.5}}}$	-	-
Channel	$g\ (mS/cm^2)$	$E\ (mV)$	p	q	α_m	β_m	α_h	β_h
M	0.75 (a.d., b.d) 1.5 (axon)	-95	1	0	$\frac{0.02}{1+e^{\frac{-V-20}{5}}}$	$0.01\cdot e^{\frac{-V-43}{18}}$	-	-
CaH	6.5 (a.d, b.d)	125	2	0	$\frac{1.6}{1+e^{-0.072\cdot(-V-5)}}$	$0.02\cdot\frac{V+8.9}{e^{\frac{V+8.9}{5}}-1}$	-	-

Table 5. Ion channel parameters for IB cells

Cell Type	Noise Amplitude $\sigma^2_{\text{ran}}\ (mA/cm^2)$
RS	0.075
FS	0.025
SOM	0.025
VIP	0
IB (axon)	0.0125
IB (soma)	0
IB (apical dendrites)	0.0025
IB (basal dendrites)	0.0025

Table 6. Random input amplitude for each cell type

in ***Traub et al.*** (***2005***) from experimental studies of rat hippocampal neurons (I_L, I_{Na}, & I_K; ***Martina and Jonas*** (***1997***); ***Martina et al.*** (***1998***)). There were 20 FS cells each in the LIP superficial layer, LIP granular layer and FEF visual module.

Our SOM cell model included a leak current I_L, a sodium current I_{Na}, a potassium current I_K, and an h-current I_{AR}. The conductance for I_{AR} was modified from experiments on guinea pig thalamic interneurons (***Huguenard and McCormick, 1992***); all other conductances were the same as for FS cells (Table 3). There were 20 SOM cells each in the LIP superficial layer, LIP deep layer, and FEF visuo-motor and visual modules.

Our VIP cell model included a leak current I_L, a sodium current I_{Na}, a potassium current I_K and a potassium D-current I_D with conductances taken from studies of guinea pig cortical neurons (***Golomb et al.*** (***2007***), Table 4). There were 20 VIP cells in the FEF visual module.

Our IB cell model consisted of a somatic compartment, an axonal compartment, and apical and basal dendritic compartments, with electrical coupling between them (Table 5). All compartments included a leak current I_L, a sodium current I_{Na}, and a potassium current I_K, whose kinetics were taken from experiments on rat hippocampal neurons (***Martina and Jonas, 1997***). The axonal compartment and both dendritic compartments also included a potassium M current (I_{KM}). Additionally, the dendritic compartments included an h-current I_{AR} (based originally on experiments on guinea pig thalamic interneurons; ***Huguenard and McCormick*** (***1992***)) and a high-threshold calcium current I_{CaH} (parameters based on studies of rat thalamocortical neurons; ***Destexhe et al.*** (***1998***)). There were 20 IB cells in the LIP module.

Each membrane channel's current I was expressed in the form

$$I = g \cdot m^p \cdot h^q \cdot (V - E)$$

where g is the channel conductance, E its reversal potential, and m and h are the gating variables, which followed the differential equation

$$\frac{dx}{dt} = \frac{1}{\tau_x} \cdot (x_\infty - x), \quad x \in \{m, h\}$$

or, in an equivalent manner

$$\frac{dx}{dt} = \alpha_x(V) \cdot (1 - x) - \beta_x(V) \cdot x, \quad x \in \{m, h\}$$

with the exception of the sodium currents for which $m = m_\infty(V)$. The expressions and values for the variables and parameters g, E, p, q, τ_m and m_∞ (or α_m and β_m), τ_h and h_∞ (or α_h and β_h) for each channel and each cell type are detailed in Tables 1 through 5.

The random current I_{ran} received by each cell followed the equation:

$$I_{ran} = \sigma^2_{ran} \cdot dW$$

where dW is Gaussian white noise of unit variance per ms, and σ^2_{ran} is the intensity of this additive white noise. The value of the parameter σ^2_{ran} used for each cell type is given in Table 6. An additional random noise of amplitude $30\mu A/cm^2$ was provided to the FEF visuo-motor module in the poor theta phase, representing arrythmic inputs from the pulvinar.

Network Connectivity

The neurons in our model interacted with each other through AMPA and $GABA_A$ synapses as well as gap junctions. The synaptic current I_{syn} received by each cell (or compartment) was the sum of the synaptic currents $I_{syn,i}$, one for each incoming synapse. The contribution of each synapse was given by the equation

$$I_{syn,i} = s_i \cdot g_i \cdot (V - E_i)$$

Synapse type	Source neuron	E_i	$\tau_{r,i}$	$\tau_{d,i}$
AMPA	RS, IB	0mV	0.125ms	1ms
NMDA	RS	0mV	12.5ms	125ms
GABA (fast inhibition)	FS	-80mV*	0.25ms	5ms
GABA (slow inhibition)	SOM, VIP	-80mV	0.25ms	20ms

Table 7. Synaptic reversal potentials and time constants for each synapse type in the network. **FS to FS synapses have a -75mV reversal potential, instead of -80mV.*

Source region		LIP							FEF vm		FEF v			
Neuron		RS	FS	SOM	g.RS	g.FS	IB	d.SOM	RS	SOM	RS	FS	SOM	VIP
Target region	Neuron													
LIP	RS	-	6.25	2	2	0.1	-	-	-	-	-	-	-	-
	FS	0.025	2	0.2	0.1	-	0.08	-	-	-	-	-	-	-
	SOM	0.225	0.4	7	-	-	0.045	-	-	-	-	-	-	-
	g.RS	-	-	-	0.5	1	-	-	-	-	-	-	-	-
	g.FS	-	-	-	1	0.3	-	1	-	-	-	-	-	-
	IB	1/60*	-	0.4	-	-	1/500	10	-	-	-	-	-	-
	d.SOM	-	-	-	-	-	-	-	0.05	-	-	-	-	-
FEF vm	RS	0.009	-	-	-	-	-	-	0.6	0.8	-	-	-	-
	SOM	0.009	-	-	-	-	-	-	0.5	-	-	-	-	-
			-	-	-	-	-	-	-	-	-	-	-	-
FEF v	RS	0.015	-	-	-	-	-	-	-	-	0.2	0.2	1	-
	FS	-	-	-	-	-	-	-	-	-	0.2	0.2	-	-
	SOM	0.025	-	-	-	-	-	-	-	-	-	-	-	0.7
	VIP	0.005	-	-	-	-	-	-	-	-	-	-	0.01	-
FEF m	RS	-	-	-	-	-	-	-	0.1**	-	0.08***	-	-	-

Table 8. Maximum conductances of the synapses in the network (in mS/cm^2). **For AMPA synapse. For NMDA : $g_i = 1/240$. **For AMPA synapse. For NMDA : $g_i = 0.01$. ***For NMDA synapse. For AMPA : $g_i = 0$.*

where g_i is the maximum conductance of the synapse and E_i is its reversal potential. The synaptic gating variable s_i depended on the rise and decay time constants of the synapse $\tau_{r,i}$ and $\tau_{d,i}$ as well as the membrane potential of the presynaptic neuron $V_{pre,i}$, according to the equation

$$s_i = -\frac{s_i}{\tau_{d,i}} + \frac{1 - s_i}{\tau_{r,i}} \cdot 0.5 \cdot \left(1 + \tanh \frac{V_{pre,i}}{10}\right)$$

The parameters chosen for each synapse type in the network are summed up in Tables 7 (for the reversal potentials, rise and decay time constants) and 8 (for the maximum conductances).

Similarly, the total gap junction current received by a cell I_{gap} was the sum of all contributions $I_{gap,i}$ received from each individual cell or compartment contacting it, described by the equation

$$I_{gap,i} = g_i \cdot (V - V_{pre,i})$$

where g_i is the maximum conductance of the gap junction and $V_{pre,i}$ is the membrane potential of the other neuron or compartment involved in the gap junction. Gap junctions were present between LIP superficial RS cells with a maximum conductance $g_i = 0.04$, between LIP superficial SOM cells with a maximum conductance $g_i = 0.2$, between LIP IB cell axons with a maximum conductance $g_i = 0.0025$, and between the different compartments of each LIP IB cell, with conductances summed up in Table 9. Of note, the maximal conductances of these gap junctions were likely larger than what would be measured for single pairs of cells *in vivo*, as is appropriate for currents in a smaller

Source compartment	Target Compartment	g (mS/cm^2)
Soma	Apical Dendrite	0.2
Soma	Basal Dendrite	0.2
Soma	Axon	0.3
Apical Dendrite	Soma	0.4
Basal Dendrite	Soma	0.4
Axon Dendrite	Soma	0.3

Table 9. Conductances of gap junctions between IB cell compartments.

Parameter	mdPul input	LIP input (only when FEF is modeled alone)	FEF input (only when LIP is modeled alone)	V4 input (only during target appearance)
Good theta f	13Hz	50Hz	25Hz	50Hz
Poor theta f	-	13Hz	-	50Hz
g_{inp}	to LIP gran. RS : 5 to LIP gran. FS : 5 to FEF vm RS : 3 to FEF vm SOM : 3	to FEF vm RS : 3 to FEF vm SOM : 3 to FEF v VIP : 2.5 to FEF v SOM : 7.5 to FEF v RS : 7.5	to LIP deep SOM : 5	to FEF v VIP : 3 to FEF v SOM : 2.5

Table 10. Nominal frequency and maximum conductances (in mS/cm^2) of inputs to the model, coming from mdPul, LIP, FEF or V4.

network.

Inputs

Some cell populations in the network received an external input current I_{inp}, following the set of equations

$$I_{\text{inp}} = s_{\text{inp}} \cdot g_{\text{inp}} \cdot (V - E_{\text{inp}})$$
$$\frac{ds_{\text{inp}}}{dt} = -\frac{s_{\text{inp}}}{\tau_{\text{d},inp}} + \frac{(1 - s_{\text{inp}})}{\tau_{\text{r},inp}} \cdot 0.5 \cdot \left(1 + \tanh \frac{V_{\text{inp}}}{10}\right)$$

where g_{inp} is the maximum conductance of the input synapse and $E_{\text{inp}} = 0mV$ is its reversal potential. The synaptic gating variable s_{inp} depended on the rise and decay time constants of the synapse $\tau_{\text{r},inp} = 0.1ms$ and $\tau_{\text{d},inp} = 0.5ms$ as well as the membrane potential of the presynaptic neuron V_{inp}.

Some cell populations also received input from neuronal populations that were not modeled explicitly (i.e., with full Hodgkin-Huxley dynamics). Each neuron in these input populations was modeled as a periodic spike train with frequency f, having inter-spike intervals uniformly randomly distributed in the interval $(0.9f, 1.1f)$, and independently chosen for each input neuron. The efferent synapses of these input populations followed the equations

$$\frac{dV_{\text{inp}}}{dt} = \frac{1}{\tau_{\text{inp}}} \cdot (V_{\text{low}} - V_{\text{inp}})$$
$$\text{on spike} : V_{\text{inp}} \leftarrow V_{\text{high}}$$

I.e., whenever a spike occurred, the membrane potentials of their synaptic targets were reset to $V_{\text{inp}} = V_{\text{high}} = 0mV$ before exponentially decaying to their baseline value $V_{\text{inp}} = V_{\text{low}} = -80mV$ with a decay time constant of $\tau_{\text{inp}} = 0.5ms$. The frequency f and conductance g_{inp} for each input synapse are given in Table 10.

Simulations

All the simulations were performed using the Brian2 libraries for Python (***Stimberg et al., 2014***), using a 4th order Runge-Kutta method to solve the differential equations defining the model, and a 0.01ms timestep. All simulations were 2 seconds long, and the first 200 ms of each simulation was discarded to remove transients. Targets were presented at cue-target delays spaced every 50ms from 200ms to 1800ms. An ensemble of 50 simulations was computed for each delay value, with randomized noise and randomized temporal jitter in the inputs. All code is available at *https://github.com/benpolletta/egly-driver-network*.

Statistics & Data Analysis

All analyses were performed in Python, with the exception of spectrograms in Figures 4C & 3C, which were computed in Matlab.

The statistics of target detection were computed for 50 simulations at each of 32 cue-target intervals (see above). A “hit" was recorded if more than half of FEF decision cells spiked at least once during the $100ms$-long window in which the target was presented. A “false alarm" was recorded if more than half of FEF decision cells spiked within a $25ms$-long window in which no target was presented. Given a hit rate H and a false alarm rate F, the sensitivity was calculated as

$$D' = z^{-1}(1-F) - z^{-1}(1-H),$$

where $z^{-1}(r)$ is defined as the inverse cumulative distribution function for the standard normal distribution on the interval $(0,1)$ (i.e., $z^{-1}(r)$ is the real number whose standard normal p-value is r), $z^{-1}(0) = z^{-1}(\epsilon)$, and $z^{-1}(1) = z^{-1}(1-\epsilon)$ for $\epsilon = 0.1$.

The θ phase was determined from synthetic mdPul α inputs, which had a period of $250ms$ and a duty cycle of $125ms$. Thus, 0° occurred at the onset of the mdPul α, and 180° occurred at the offset of mdPul α. The LIP β_1 phase during the poor θ phase was determined from the timing of superficial RS cells spiking (RS cells spiking was considered to be at 0°), assuming a β_1 frequency of 10 Hz.

LIP LFPs were computed by averaging the membrane potentials of superficial RS cells; FEF visuo-motor LFPs were computed by averaging the membrane potentials of visuo-motor RS cells.

Power spectra were calculated using SciPy’s *signal.periodogram* with a flat top window. The spectrograms in Figures 4C & 3C were calculated from LFPs taken from a single 2 second simulation, via convolution with complex Morlet wavelets (obtained with Matlab’s *dftfilt3*) with frequencies between 9 and 60 Hz; the width of these wavelets was linearly interpolated from 4 cycles at 9 Hz to 12 cycles at 60 Hz.

Funding Information

This research has been supported by funding from the NIH/NIMH grant P50 MH109429 on Neurobiology and Dynamics of Active Sensing.

References

Askew CE, Lopez AJ, Wood MA, Metherate R. Nicotine excites VIP interneurons to disinhibit pyramidal neurons in auditory cortex. Synapse. 2019; 73(9):e22116.

Audette NJ, Urban-Ciecko J, Matsushita M, Barth AL. POm Thalamocortical Input Drives Layer-Specific Microcircuits in Somatosensory Cortex. Cerebral Cortex. 2018; 28(4):1312–1328. https://doi.org/10.1093/cercor/bhx044, doi: 10.1093/cercor/bhx044.

Beierlein M, Gibson JR, Connors BW. A network of electrically coupled interneurons drives synchronized inhibition in neocortex. Nature neuroscience. 2000; 3(9):904–910.

Benedetto A, Morrone MC, Tomassini A. The Common Rhythm of Action and Perception. Journal of Cognitive Neuroscience. 2020 Feb; 32(2):187–200. https://doi.org/10.1162/jocn_a_01436, doi: 10.1162/jocn_a_01436.

Bisley JW, Mirpour K, Arcizet F, Ong WS. The role of the lateral intraparietal area in orienting attention and its implications for visual search. European Journal of Neuroscience. 2011 Jun; 33(11):1982–1990. https://doi.org/10.1111/j.1460-9568.2011.07700.x, doi: 10.1111/j.1460-9568.2011.07700.x.

Buschman TJ, Miller EK. Top-Down Versus Bottom-Up Control of Attention in the Prefrontal and Posterior Parietal Cortices. Science. 2007 Mar; 315(5820):1860–1862. https://doi.org/10.1126/science.1138071, doi: 10.1126/science.1138071.

Corbetta M, Akbudak E, Conturo TE, Snyder AZ, Ollinger JM, Drury HA, Linenweber MR, Petersen SE, Raichle ME, Essen DCV, Shulman GL. A Common Network of Functional Areas for Attention and Eye Movements. Neuron. 1998 Oct; 21(4):761–773. https://doi.org/10.1016/s0896-6273(00)80593-0, doi: 10.1016/s0896-6273(00)80593-0.

Cruikshank SJ, Urabe H, Nurmikko AV, Connors BW. Pathway-Specific Feedforward Circuits between Thalamus and Neocortex Revealed by Selective Optical Stimulation of Axons. Neuron. 2010 Jan; 65(2):230–245. https://doi.org/10.1016/j.neuron.2009.12.025, doi: 10.1016/j.neuron.2009.12.025.

Del Molino LCG, Yang GR, Mejias JF, Wang XJ. Paradoxical response reversal of top-down modulation in cortical circuits with three interneuron types. Elife. 2017; 6:e29742.

Destexhe A, Neubig M, Ulrich D, Huguenard J. Dendritic low-threshold calcium currents in thalamic relay cells. Journal of Neuroscience. 1998; 18(10):3574–3588.

Dipoppa M, Ranson A, Krumin M, Pachitariu M, Carandini M, Harris KD. Vision and locomotion shape the interactions between neuron types in mouse visual cortex. Neuron. 2018; 98(3):602–615.

Džaja D, Hladnik A, Bičanić I, Baković M, Petanjek Z. Neocortical calretinin neurons in primates: increase in proportion and microcircuitry structure. Frontiers in neuroanatomy. 2014; 8:103.

Fanselow EE, Richardson KA, Connors BW. Selective, state-dependent activation of somatostatin-expressing inhibitory interneurons in mouse neocortex. Journal of neurophysiology. 2008; 100(5):2640–2652.

Fiebelkorn IC, Kastner S. The Puzzling Pulvinar. Neuron. 2019 Jan; 101(2):201–203. https://doi.org/10.1016/j.neuron.2018.12.032, doi: 10.1016/j.neuron.2018.12.032.

Fiebelkorn IC, Kastner S. A Rhythmic Theory of Attention. Trends in Cognitive Sciences. 2019 Feb; 23(2):87–101. https://doi.org/10.1016/j.tics.2018.11.009, doi: 10.1016/j.tics.2018.11.009.

Fiebelkorn IC, Pinsk MA, Kastner S. A Dynamic Interplay within the Frontoparietal Network Underlies Rhythmic Spatial Attention. Neuron. 2018 Aug; 99(4):842–853.e8. https://doi.org/10.1016/j.neuron.2018.07.038, doi: 10.1016/j.neuron.2018.07.038.

Fiebelkorn IC, Pinsk MA, Kastner S. The mediodorsal pulvinar coordinates the macaque fronto-parietal network during rhythmic spatial attention. Nature Communications. 2019 Jan; 10(1). https://doi.org/10.1038/s41467-018-08151-4, doi: 10.1038/s41467-018-08151-4.

Fiebelkorn IC, Saalmann YB, Kastner S. Rhythmic Sampling within and between Objects despite Sustained Attention at a Cued Location. Current Biology. 2013 Dec; 23(24):2553–2558. https://doi.org/10.1016/j.cub.2013.10.063, doi: 10.1016/j.cub.2013.10.063.

Fries P. Neuronal Gamma-Band Synchronization as a Fundamental Process in Cortical Computation. Annual Review of Neuroscience. 2009 Jun; 32(1):209–224. https://doi.org/10.1146/annurev.neuro.051508.135603, doi: 10.1146/annurev.neuro.051508.135603.

Gaillard C, Hassen SBH, Bello FD, Bihan-Poudec Y, VanRullen R, Hamed SB. Prefrontal attentional saccades explore space rhythmically. Nature Communications. 2020 Feb; 11(1). https://doi.org/10.1038/s41467-020-14649-7, doi: 10.1038/s41467-020-14649-7.

Garrett M, Manavi S, Roll K, Ollerenshaw DR, Groblewski PA, Ponvert ND, Kiggins JT, Casal L, Mace K, Williford A, et al. Experience shapes activity dynamics and stimulus coding of VIP inhibitory cells. Elife. 2020; 9:e50340.

Gelastopoulos A, Whittington MA, Kopell NJ. Parietal low beta rhythm provides a dynamical substrate for a working memory buffer. Proceedings of the National Academy of Sciences. 2019 Aug; 116(33):16613–16620. https://doi.org/10.1073/pnas.1902305116, doi: 10.1073/pnas.1902305116.

Golomb D, Donner K, Shacham L, Shlosberg D, Amitai Y, Hansel D. Mechanisms of firing patterns in fast-spiking cortical interneurons. PLoS Computational Biology. 2007; 3(8):e156.

Gregoriou GG, Gotts SJ, Desimone R. Cell-Type-Specific Synchronization of Neural Activity in FEF with V4 during Attention. Neuron. 2012 Feb; 73(3):581–594. https://doi.org/10.1016/j.neuron.2011.12.019, doi: 10.1016/j.neuron.2011.12.019.

Gutierrez C, Cola MG, Seltzer B, Cusick C. Neurochemical and connectional organization of the dorsal pulvinar complex in monkeys. The Journal of Comparative Neurology. 2000 Mar; 419(1):61–86. https://doi.org/10.1002/(sici)1096-9861(20000327)419:1<61::aid-cne4>3.0.co;2-i, doi: 10.1002/(sici)1096-9861(20000327)419:1<61::aid-cne4>3.0.co;2-i.

Halassa MM, Kastner S. Thalamic functions in distributed cognitive control. Nature Neuroscience. 2017 Nov; 20(12):1669–1679. https://doi.org/10.1038/s41593-017-0020-1, doi: 10.1038/s41593-017-0020-1.

Helfrich RF, Fiebelkorn IC, Szczepanski SM, Lin JJ, Parvizi J, Knight RT, Kastner S. Neural Mechanisms of Sustained Attention Are Rhythmic. Neuron. 2018 Aug; 99(4):854–865.e5. https://doi.org/10.1016/j.neuron.2018.07.032, doi: 10.1016/j.neuron.2018.07.032.

Hertäg L, Sprekeler H. Learning prediction error neurons in a canonical interneuron circuit. Elife. 2020; 9:e57541.

Hodge RD, Bakken TE, Miller JA, Smith KA, Barkan ER, Graybuck LT, Close JL, Long B, Johansen N, Penn O, et al. Conserved cell types with divergent features in human versus mouse cortex. Nature. 2019; 573(7772):61–68.

Hu H, Agmon A. Properties of precise firing synchrony between synaptically coupled cortical interneurons depend on their mode of coupling. Journal of neurophysiology. 2015; 114(1):624–637.

Huang P, Xiang X, Chen X, Li H. Somatostatin neurons govern theta oscillations induced by salient visual signals. Cell Reports. 2020; 33(8):108415.

Huguenard JR, McCormick DA. Simulation of the currents involved in rhythmic oscillations in thalamic relay neurons. Journal of neurophysiology. 1992; 68(4):1373–1383.

Jaramillo J, Mejias JF, Wang XJ. Engagement of Pulvino-cortical Feedforward and Feedback Pathways in Cognitive Computations. Neuron. 2019 Jan; 101(2):321–336.e9. https://doi.org/10.1016/j.neuron.2018.11.023, doi: 10.1016/j.neuron.2018.11.023.

Kalmbach BE, Buchin A, Long B, Close J, Nandi A, Miller JA, Bakken TE, Hodge RD, Chong P, de Frates R, et al. h-Channels contribute to divergent intrinsic membrane properties of supragranular pyramidal neurons in human versus mouse cerebral cortex. Neuron. 2018; 100(5):1194–1208.

Karnani MM, Jackson J, Ayzenshtat I, Sichani AH, Manoocheri K, Kim S, Yuste R. Opening Holes in the Blanket of Inhibition: Localized Lateral Disinhibition by VIP Interneurons. Journal of Neuroscience. 2016 Mar; 36(12):3471–3480. https://doi.org/10.1523/jneurosci.3646-15.2016, doi: 10.1523/jneurosci.3646-15.2016.

Kastner S, Fiebelkorn IC, Eradath MK. Dynamic pulvino-cortical interactions in the primate attention network. Current Opinion in Neurobiology. 2020 Dec; 65:10–19. https://doi.org/10.1016/j.conb.2020.08.002, doi: 10.1016/j.conb.2020.08.002.

Keller AJ, Dipoppa M, Roth MM, Caudill MS, Ingrosso A, Miller KD, Scanziani M. A disinhibitory circuit for contextual modulation in primary visual cortex. Neuron. 2020; 108(6):1181–1193.

Krabbe S, Paradiso E, d'Aquin S, Bitterman Y, Courtin J, Xu C, Yonehara K, Markovic M, Müller C, Eichlisberger T, et al. Adaptive disinhibitory gating by VIP interneurons permits associative learning. Nature neuroscience. 2019; 22(11):1834–1843.

Kramer MA, Roopun AK, Carracedo LM, Traub RD, Whittington MA, Kopell NJ. Rhythm Generation through Period Concatenation in Rat Somatosensory Cortex. PLoS Computational Biology. 2008 Sep; 4(9):e1000169. https://doi.org/10.1371/journal.pcbi.1000169, doi: 10.1371/journal.pcbi.1000169.

Krienen FM, Goldman M, Zhang Q, CH del Rosario R, Florio M, Machold R, Saunders A, Levandowski K, Zaniewski H, Schuman B, et al. Innovations present in the primate interneuron repertoire. Nature. 2020; 586(7828):262–269.

Landau AN, Fries P. Attention Samples Stimuli Rhythmically. Current Biology. 2012 Jun; 22(11):1000–1004. https://doi.org/10.1016/j.cub.2012.03.054, doi: 10.1016/j.cub.2012.03.054.

Lee AT, Cunniff MM, See JZ, Wilke SA, Luongo FJ, Ellwood IT, Ponnavolu S, Sohal VS. VIP interneurons contribute to avoidance behavior by regulating information flow across hippocampal-prefrontal networks. Neuron. 2019; 102(6):1223–1234.

Lee JH, Koch C, Mihalas S. A computational analysis of the function of three inhibitory cell types in contextual visual processing. Frontiers in Computational Neuroscience. 2017; 11:28.

Lee JH, Whittington MA, Kopell NJ. Top-Down Beta Rhythms Support Selective Attention via Interlaminar Interaction: A Model. PLoS Computational Biology. 2013 Aug; 9(8):e1003164. https://doi.org/10.1371/journal.pcbi.1003164, doi: 10.1371/journal.pcbi.1003164.

Martina M, Jonas P. Functional differences in Na+ channel gating between fast-spiking interneurones and principal neurones of rat hippocampus. The Journal of physiology. 1997; 505(Pt 3):593.

Martina M, Schultz JH, Ehmke H, Monyer H, Jonas P. Functional and molecular differences between voltage-gated K+ channels of fast-spiking interneurons and pyramidal neurons of rat hippocampus. Journal of Neuroscience. 1998; 18(20):8111–8125.

Miller EK, Buschman TJ. Cortical circuits for the control of attention. Current Opinion in Neurobiology. 2013 Apr; 23(2):216–222. https://doi.org/10.1016/j.conb.2012.11.011, doi: 10.1016/j.conb.2012.11.011.

Millman DJ, Ocker GK, Caldejon S, Larkin JD, Lee EK, Luviano J, Nayan C, Nguyen TV, North K, Seid S, et al. VIP interneurons in mouse primary visual cortex selectively enhance responses to weak but specific stimuli. Elife. 2020; 9:e55130.

Moore T, Fallah M. Control of eye movements and spatial attention. Proceedings of the National Academy of Sciences. 2001 Jan; 98(3):1273–1276. https://doi.org/10.1073/pnas.98.3.1273, doi: 10.1073/pnas.98.3.1273.

Pogosyan A, Gaynor LD, Eusebio A, Brown P. Boosting Cortical Activity at Beta-Band Frequencies Slows Movement in Humans. Current Biology. 2009 Oct; 19(19):1637–1641. https://doi.org/10.1016/j.cub.2009.07.074, doi: 10.1016/j.cub.2009.07.074.

Povysheva NV, Zaitsev AV, Rotaru DC, Gonzalez-Burgos G, Lewis DA, Krimer LS. Parvalbumin-positive basket interneurons in monkey and rat prefrontal cortex. Journal of neurophysiology. 2008; 100(4):2348–2360.

Romanski LM, Giguere M, Bates JF, Goldman-Rakic PS. Topographic organization of medial pulvinar connections with the prefrontal cortex in the rhesus monkey. The Journal of Comparative Neurology. 1997 Mar; 379(3):313–332. https://doi.org/10.1002/(sici)1096-9861(19970317)379:3<313::aid-cne1>3.0.co;2-6, doi: 10.1002/(sici)1096-9861(19970317)379:3<313::aid-cne1>3.0.co;2-6.

Roopun AK, Kramer MA, Carracedo LM, Kaiser M, Davies CH, Traub RD, Kopell NJ, Whittington MA. Period concatenation underlies interactions between gamma and beta rhythms in neocortex. Frontiers in Cellular Neuroscience. 2008; 2. https://doi.org/10.3389/neuro.03.001.2008, doi: 10.3389/neuro.03.001.2008.

Rudy B, Fishell G, Lee S, Hjerling-Leffler J. Three groups of interneurons account for nearly 100% of neocortical GABAergic neurons. Developmental neurobiology. 2011; 71(1):45–61.

Saalmann YB, Kastner S. Cognitive and Perceptual Functions of the Visual Thalamus. Neuron. 2011 Jul; 71(2):209–223. https://doi.org/10.1016/j.neuron.2011.06.027, doi: 10.1016/j.neuron.2011.06.027.

Safari MS, Mirnajafi-Zadeh J, Hioki H, Tsumoto T. Parvalbumin-expressing interneurons can act solo while somatostatin-expressing interneurons act in chorus in most cases on cortical pyramidal cells. Scientific Reports. 2017; 7(1):1–14.

Selemon L, Goldman-Rakic P. Common cortical and subcortical targets of the dorsolateral prefrontal and posterior parietal cortices in the rhesus monkey: evidence for a distributed neural network subserving spatially guided behavior. The Journal of Neuroscience. 1988 Nov; 8(11):4049–4068. https://doi.org/10.1523/jneurosci.08-11-04049.1988, doi: 10.1523/jneurosci.08-11-04049.1988.

Silberberg G, Markram H. Disynaptic inhibition between neocortical pyramidal cells mediated by Martinotti cells. Neuron. 2007; 53(5):735–746.

Song K, Meng M, Chen L, Zhou K, Luo H. Behavioral Oscillations in Attention: Rhythmic α Pulses Mediated through θ Band. The Journal of Neuroscience. 2014 Apr; 34(14):4837–4844. https://doi.org/10.1523/jneurosci.4856-13.2014, doi: 10.1523/jneurosci.4856-13.2014.

Stimberg M, Goodman DF, Benichoux V, Brette R. Equation-oriented specification of neural models for simulations. Frontiers in Neuroinformatics. 2014; 8.

Traub RD, Contreras D, Cunningham MO, Murray H, LeBeau FE, Roopun A, Bibbig A, Wilent WB, Higley MJ, Whittington MA. Single-column thalamocortical network model exhibiting gamma oscillations, sleep spindles, and epileptogenic bursts. Journal of neurophysiology. 2005; 93(4):2194–2232.

Tremblay R, Lee S, Rudy B. GABAergic Interneurons in the Neocortex: From Cellular Properties to Circuits. Neuron. 2016 Jul; 91(2):260–292. https://doi.org/10.1016/j.neuron.2016.06.033, doi: 10.1016/j.neuron.2016.06.033.

VanRullen R, Carlson T, Cavanagh P. The blinking spotlight of attention. Proceedings of the National Academy of Sciences. 2007 Nov; 104(49):19204–19209. https://doi.org/10.1073/pnas.0707316104, doi: 10.1073/pnas.0707316104.

Veit J, Mossing DP, Adesnik H. VIP neurons desynchronize cortical assemblies. bioRxiv. 2021; .

Wall NR, De La Parra M, Sorokin JM, Taniguchi H, Huang ZJ, Callaway EM. Brain-wide maps of synaptic input to cortical interneurons. Journal of Neuroscience. 2016; 36(14):4000–4009.

Yang GR, Murray JD, Wang XJ. A dendritic disinhibitory circuit mechanism for pathway-specific gating. Nature communications. 2016; 7(1):1–14.

Zhang S, Xu M, Kamigaki T, Do JPH, Chang WC, Jenvay S, Miyamichi K, Luo L, Dan Y. Long-range and local circuits for top-down modulation of visual cortex processing. Science. 2014 Aug; 345(6197):660–665. https://doi.org/10.1126/science.1254126, doi: 10.1126/science.1254126.

Zhang Y, Chen Y, Bressler SL, Ding M. Response preparation and inhibition: The role of the cortical sensorimotor beta rhythm. Neuroscience. 2008 Sep; 156(1):238–246. https://doi.org/10.1016/j.neuroscience.2008.06.061, doi: 10.1016/j.neuroscience.2008.06.061.

Zhou H, Schafer RJ, Desimone R. Pulvinar-Cortex Interactions in Vision and Attention. Neuron. 2016 Jan; 89(1):209–220. https://doi.org/10.1016/j.neuron.2015.11.034, doi: 10.1016/j.neuron.2015.11.034.

Zhou N, Masterson SP, Damron JK, Guido W, Bickford ME. The Mouse Pulvinar Nucleus Links the Lateral Extrastriate Cortex, Striatum, and Amygdala. The Journal of Neuroscience. 2018 Jan; 38(2):347–362. https://doi.org/10.1523/jneurosci.1279-17.2017, doi: 10.1523/jneurosci.1279-17.2017.

Appendix

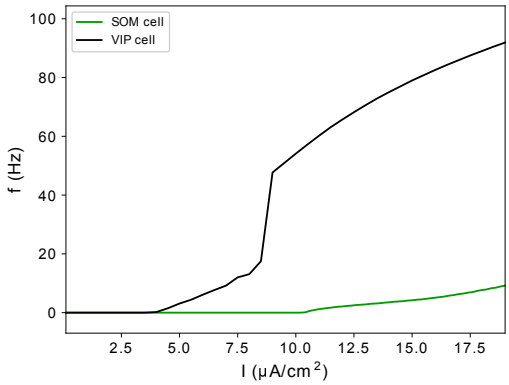

Figure S1. **f-I curves of model SOM and VIP cells**.

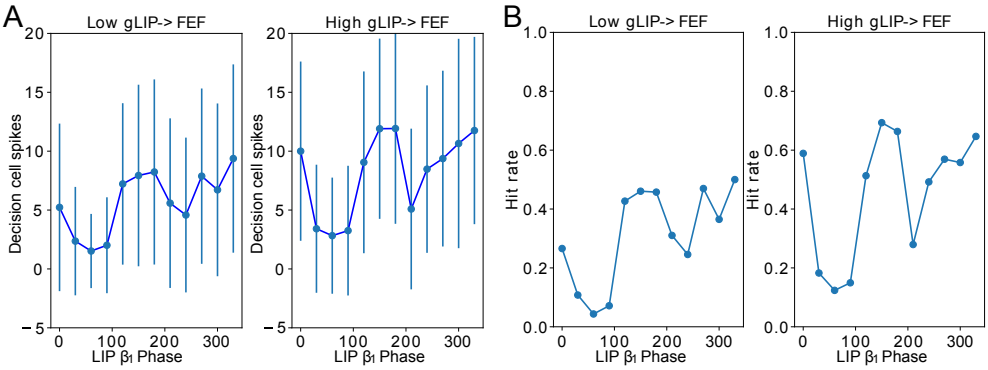

Figure S2. **Conductance of LIP→FEF synapses increases dependence of decision cell spiking and hit rate on LIP β_1 phase. A. Decision cell spiking (mean±SD) as a function of LIP β_1 phase (see Methods). B. Hit rate as a function of LIP β_1 phase.**

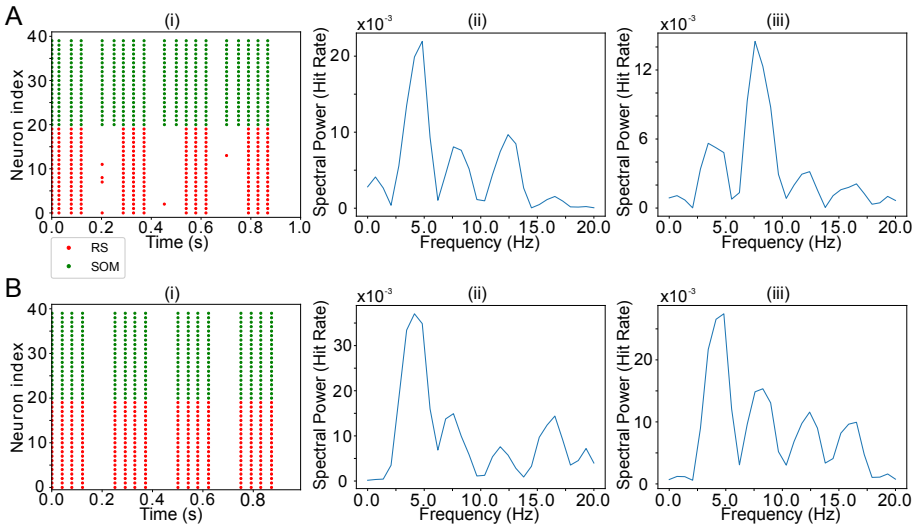

Figure S3. **8 Hz hit-rate rhythmicity depends on FEF visuo-motor dynamics via noisy input drive. A. Network dynamics with noisy mdPul input.** i. Raster plot of FEF visuomotor module. ii. Spectral power of hit rates for $g_{\text{LIP}\to\text{FEF}} = 0.15$. iii. Spectral power of hit rates for $g_{\text{LIP}\to\text{FEF}} = 0.2$. **B. Network dynamics without noise in mdPul input.** Subplots are as in A.

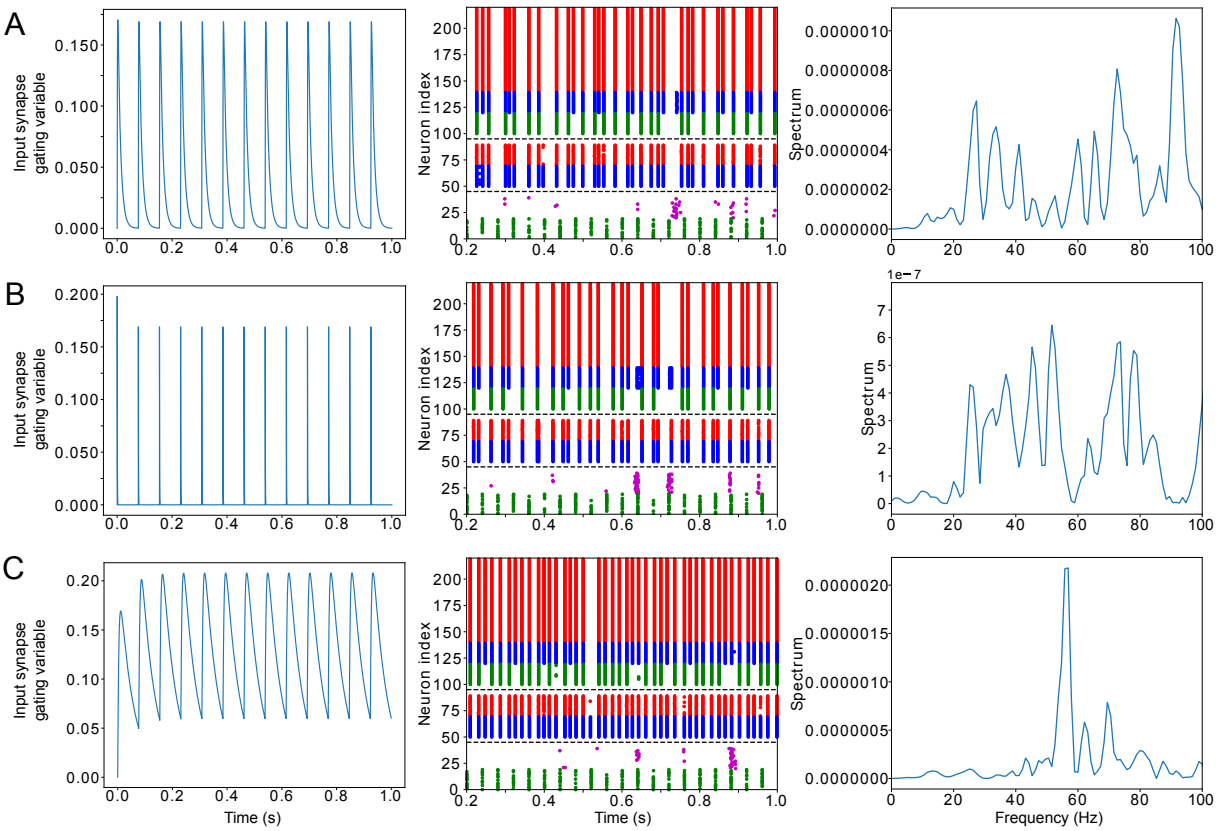

Figure S4. LIP good θ phase γ can be obtained with mdPul α stimulation of various widths. A. LIP good θ phase behavior with mdPul input synapse timescales of $\tau_{rise} = 2ms$ and $\tau_{decay} = 10ms$, the default values used throughout this paper. Left: input synapse opening variable of a 1s-long simulation. Middle: Raster plot of a 1s-long simulation. Right: power spectrum of the LFP generated by the network in this 1s-long simulation. **B. LIP good θ phase behavior with shorter mdPul input synapse timescales of $\tau_{rise} = 0.1ms$ and $\tau_{decay} = 0.5ms$.** Subplots are as described for A. **C. LIP good θ phase behavior with longer mdPul input synapse timescales of $\tau_{rise} = 10ms$ and $\tau_{decay} = 50ms$.** Subplots are as described for A.

Influence of Tonic Excitation on LIP Behavior

The tonic excitation range for the LIP module to exhibit behavior matching experimental observations is rather broad (between -7 and $2uA/cm^2$ for FS cells and between -25 and 15 uA/cm^2 for RS cells), but choosing excitation levels out of this range can disturb both the β_1 rhythm during poor θ phase and the γ rhythm during good θ phase. Excessive tonic excitation of input layer FS cells—which inhibit superficial RS cells (see LIP model, Figure 3A)—disturbs the β_1 rhythm by preventing superficial RS cell spiking (Figure S6A), while insufficient tonic drive to input layer FS cells disturbs the β_1 rhythm by allowing input RS cells to spike and entrain the superficial layer (Figure S6B). Finally, insufficient tonic excitation to input layer RS cells disturbs the good θ phase γ rhythm, rendering RS cells unable to sustain their activity outside the windows of disinhibition provided by deep SOM cells spiking (Figure S6C).

Influence of Input Parameters on FEF Visuo-Motor Module Behavior

Our explorations indicate that a broad range of tonic excitation levels result in RS cell quiescence during the poor θ phase and β_2 rhythmicity in RS and SOM cells during the good θ phase (S8). Too much tonic excitation to RS cells compared to SOM cells (Figure S8A) results in RS cell firing during the poor θ phase despite SOM cell inhibition, while too little tonic excitation to RS cells compared to SOM cells results in the RS cells being unable to take control of SOM cells outside of the windows of disinhibition provided by VIP cells in the good θ phase, and a resulting β_1 (rather than β_2) rhythm.

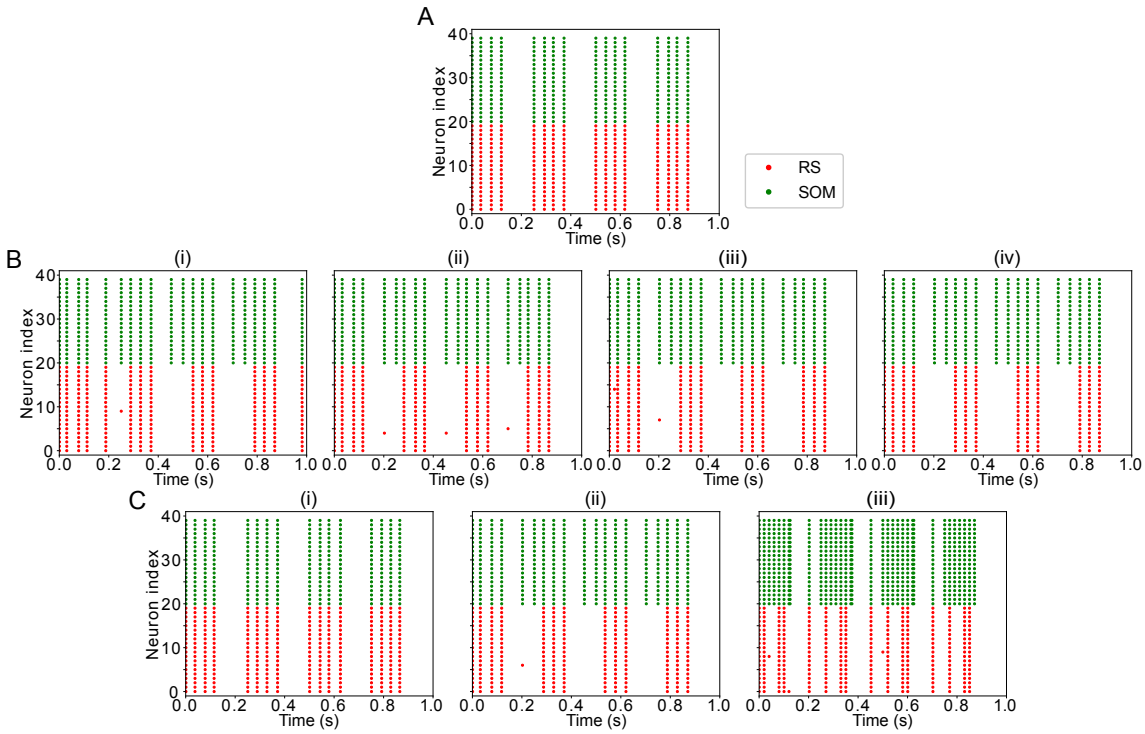

Figure S5. FEF visuo-motor module good θ phase behavior is influenced by LIP input properties. A. Raster plot of FEF visuo-motor behavior without LIP input during a 1s-long simulation with alternating good and poor θ phase (the good θ phase β_2 rhythm gets slower). B. Raster plots of FEF visuo-motor behavior with various LIP input frequencies during 1s-long simulations with alternating good and poor θ phase. (i) 5Hz LIP input slows the good θ phase β_2 rhythm. (ii) 13Hz LIP input slows the good θ phase β_2 rhythm. (iii) 25Hz LIP input preserves the good θ phase β_2 rhythm. (iv) 150Hz LIP input speeds the good θ phase β_2 rhythm. **C. Raster plots of FEF visuo-motor behavior with various LIP input strengths during 1s-long simulations with alternating good and poor θ phase.** (i) $1mS/cm^2$ input. (ii) $5mS/cm^2$ input. (iii) $15mS/cm^2$ input.

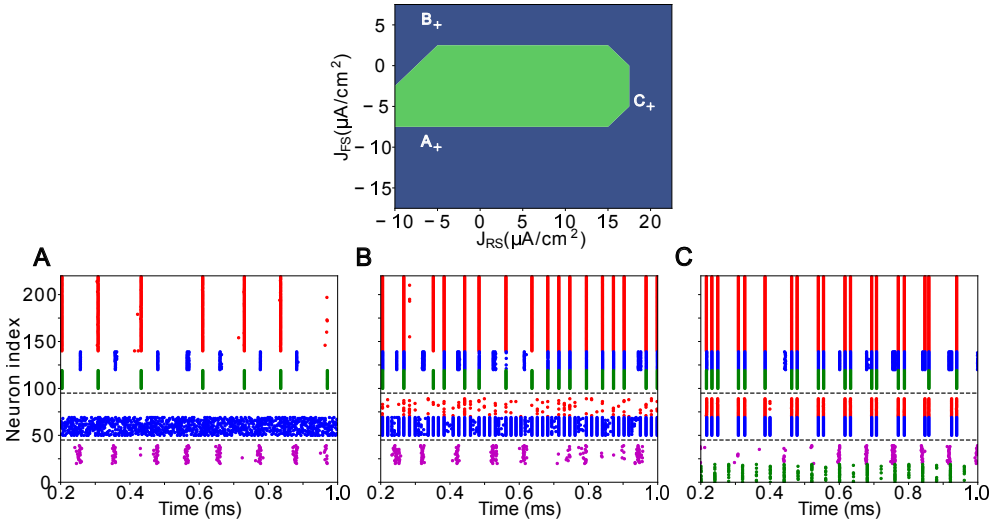

Figure S6. LIP good and poor θ phase behavior depends on input layer tonic excitation. Top: Appropriate tonic excitation range needed to obtain a γ rhythm in the good θ phase and β_1 rhythm in the poor θ phase. The crosses indicate the sets of values used in simulations for A, B, and C below. **A. Excessive tonic excitation to input layer FS cells disturbs the poor θ phase β_1 rhythm by preventing superficial RS cells spikes. B. Having insufficient tonic excitation to input layer FS cells disturbs the poor θ phase β_1 rhythm by allowing input RS cells to spike and entrain the superficial layer. C. Having insufficient tonic excitation to input layer RS cells disturbs the good θ phase γ rhythm.**

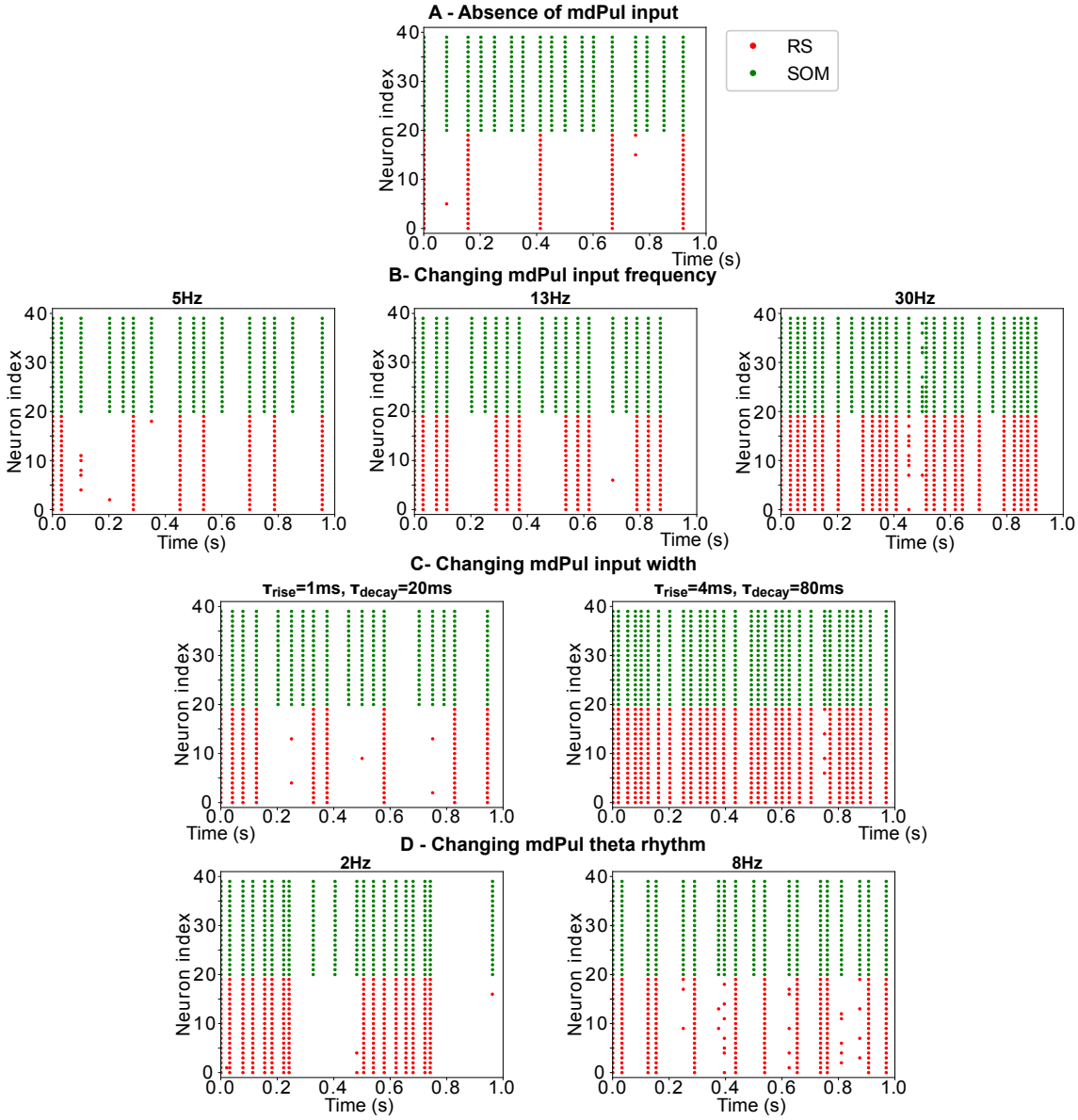

Figure S7. FEF visuo-motor module good θ phase behavior is influenced by mdPul input properties. A. Raster plot of FEF visuo-motor behavior without mdPul input during a 1s-long simulation with alternating good and poor θ phase (no β_2 rhythm appears in the good θ phase). B. Raster plots of FEF visuo-motor behavior with various mdPul input frequencies, during a 1s-long simulations with alternating good and poor θ phase. Left: 5Hz mdPul input (the β_2 rhythm is not sustained). Middle: 9Hz mdPul input (the β_2 rhythm is not sustained). Right: 30Hz mdPul input (the β_2 rhythm is preserved). **C. Raster plot of FEF visuo-motor good θ phase behavior with altered mdPul input synapse timescales.** Left: $\tau_{rise} = 0.1ms$ and $\tau_{decay} = 0.5ms$ (the β_2 rhythm is preserved). Right: $\tau_{rise} = 10ms$ and $\tau_{decay} = 50ms$ (the β_2 rhythm is preserved). **D. Raster plots of FEF visuo-motor behavior, during a 1s-long simulations with alternating good and poor θ phase with various frequencies.** Left: 2Hz "theta" input (the β_2 rhythm is sustained). Right: 8Hz "theta" input (the β_2 rhythm is not sustained).

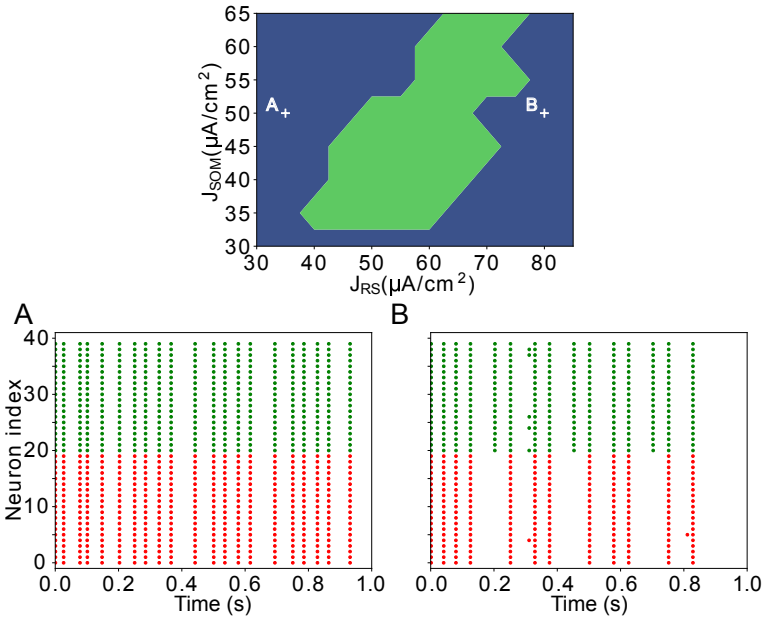

Figure S8. **FEF visuo-motor module good and poor θ phase behavior depends on the tonic excitation given to RS and SOM cells** Top: Appropriate tonic excitation range needed to obtain a β_2 rhythm in the good θ phase and quiet RS cells in the poor θ phase. The crosses indicate the two sets of values used in simulations for A and B below. **A. Having insufficient tonic excitation to SOM cells disturbs the poor θ phase by allowing RS cells spikes. B. Having excessive tonic excitation to SOM cells disturbs the good θ phase β_2 rhythm by silencing RS cells outside the disinhibition windows provided by VIP cells.**